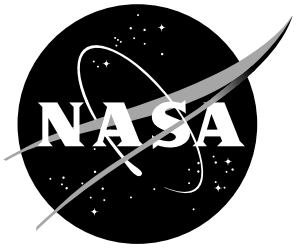
NASA–TM–20260007850



Summary of the Vertical Lift Proprotor Noise Test

Colin M. Stutz, Nikolas S. Zawodny, and Mary L. Houston
NASA Langley Research Center
Hampton, VA

September 2026

NASA STI Program. . . in Profile

Since its founding, NASA has been dedicated to the advancement of aeronautics and space science. The NASA scientific and technical information (STI) program plays a key part in helping NASA maintain this important role.

The NASA STI Program operates under the auspices of the Agency Chief Information Officer. It collects, organizes, provides for archiving, and disseminates NASA's STI. The NASA STI Program provides access to the NASA Aeronautics and Space Database and its public interface, the NASA Technical Report Server, thus providing one of the largest collection of aeronautical and space science STI in the world. Results are published in both non-NASA channels and by NASA in the NASA STI Report Series, which includes the following report types:

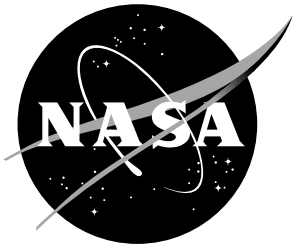
- TECHNICAL PUBLICATION. Reports of completed research or a major significant phase of research that present the results of NASA programs and include extensive data or theoretical analysis. Includes compilations of significant scientific and technical data and information deemed to be of continuing reference value. NASA counterpart of peer-reviewed formal professional papers, but having less stringent limitations on manuscript length and extent of graphic presentations.
- TECHNICAL MEMORANDUM. Scientific and technical findings that are preliminary or of specialized interest, e.g., quick release reports, working papers, and bibliographies that contain minimal annotation. Does not contain extensive analysis.
- CONTRACTOR REPORT. Scientific and technical findings by NASA-sponsored contractors and grantees.
- CONFERENCE PUBLICATION. Collected papers from scientific and technical conferences, symposia, seminars, or other meetings sponsored or co-sponsored by NASA.
- SPECIAL PUBLICATION. Scientific, technical, or historical information from NASA programs, projects, and missions, often concerned with subjects having substantial public interest.
- TECHNICAL TRANSLATION. English-language translations of foreign scientific and technical material pertinent to NASA's mission.

Specialized services also include organizing and publishing research results, distributing specialized research announcements and feeds, providing information desk and personal search support, and enabling data exchange services.

For more information about the NASA STI Program, see the following:

- Access the NASA STI program home page at `http://www.sti.nasa.gov`
- E-mail your question to `help@sti.nasa.gov`
- Phone the NASA STI Information Desk at 757-864-9658
- Write to:
  NASA STI Information Desk
  Mail Stop 148
  NASA Langley Research Center
  Hampton, VA 23681-2199

NASA–TM–20260007850



Summary of the Vertical Lift Proprotor Noise Test

Colin M. Stutz, Nikolas S. Zawodny, and Mary L. Houston
NASA Langley Research Center
Hampton, VA

National Aeronautics and
Space Administration

Langley Research Center
Hampton, Virginia 23681-2199

September 2026

Acknowledgments

The authors would like to thank the teams that were critical to the success of this test. These include the engineer and technician staffs of the Low Speed Aeroacoustic Wind Tunnel and the 14- by 22-Foot Subsonic Tunnel. Additionally, the authors would like to thank the Icing Research Group at NASA's Glenn Research Center for providing the blades for the scaling study, Prof. Nathan Alexander for providing the blade and hub geometries for CoPTR, and Joby Aviation for publicly releasing the CoPTR blade design. Support was also provided by the Durability, Damage Tolerance, and Reliability Branch and the Flight Vehicle Acoustics Branch at NASA's Langley Research Center. This test was funded by the Revolutionary Vertical Lift Technology Project and the test documentation effort by the Subsonic Vehicle Technologies and Tools project.

The use of trademarks or names of manufacturers in this report is for accurate reporting and does not constitute an official endorsement, either expressed or implied, of such products or manufacturers by the National Aeronautics and Space Administration.

Available from:

NASA STI Program / Mail Stop 148
NASA Langley Research Center
Hampton, VA 23681-2199
Fax: 757-864-6500

Abstract

Urban Air Mobility (UAM) vectored thrust vehicle platforms present the challenges of requiring propulsors to operate in both vertical takeoff and landing (VTOL) as well as axial forward flight. Such vectored thrust vehicles must also contend with the transition flight corridors of departure and approach. Transitional flight conditions create complex aerodynamic interactions, which lead to performance and acoustic characteristics that are difficult to predict numerically. The Vertical Lift Proprotor Noise Test (VLPNT) was a wind tunnel testing campaign in the NASA Langley Research Center's 14- by 22-Foot Subsonic Tunnel aimed at measuring the aerodynamic performance and acoustic behavior of proprotors operating at conditions representative of those from vectored thrust UAM vehicles with articulating propulsors. Another objective of the VLPNT was to conduct a scaling investigation on a subset of the tested proprotor geometries in an effort to identify low-Reynolds number impacts on performance and acoustics. This report documents the test campaign and the resulting data that are available to the community.

Contents

1 Introduction **5**

2 Description of Test Articles **6**

3 Description of Test **8**
3.1 14- by 22-Foot Subsonic Tunnel 8
3.2 Test Matrix 9

4 Instrumentation **10**
4.1 Propeller Test Stand (PTS) 10
4.2 Microphone Instrumentation 11
4.2.1 Grid Array 11
4.2.2 Phased Array 12
4.3 Load Measurements 13

5 Results **15**
5.1 Performance Data 15
5.1.1 Validation of COPR5-L Data from VLPPT 15
5.1.2 Large-envelope Validation Data Set 15
5.1.3 Proprotor Scaling Study 17
5.1.4 Airfoil Self Noise Data Set 18
5.2 Acoustic Data 18
5.2.1 Data Corrections 18
5.2.2 Periodic Averaging 19
5.2.3 Grid Array 20
5.2.4 Phased Array 21
5.2.5 Additional Observations 22

6 Data Availability **22**
6.1 Data Files 23
6.2 Blade Geometries 24

7 Concluding Remarks **25**

List of Tables

1 Summary of test articles. 28
2 Radial locations of collective angle settings. 28
3 Collected data sets for COPR-L configurations, $D = 24$". 28
4 Collected data sets for COPR-G configurations. 29
5 Collected data sets for CoPTR blades, $D = 24$", $N_b = 5$. 29
6 Collected data sets for KA1Gen blades, $D = 24$", $N_b = 3$. 29
7 Phased array coordinates, where $+x$ is streamwise, $+y$ is up, and $+z$ is into the array face. 30
8 Speaker waveforms. 31
9 Propeller vs. Rotor Dimensionless Parameters. 32
10 Guide for Applying Microphone Corrections. 33
11 Data subset to be hosted online. 34
12 Description of Microphone Data Files. 35
13 Description of Steady Load Data Files. 36
14 Description of Unsteady Load Data Files. 37

List of Figures

1 COPR-L blades in (a) clean COPR5-L configuration without a spinner and COPR3-L with (b) no trip dots, (c) 3.1 mil trip dots, (d) 6 mil trip dots, and (e) 9.9 mil trip dots without a spinner. (*Source: NASA*) 38
2 COPR-G configurations: (a) 36" COPR2-G, (b) 24" COPR2-G, (c) 28" COPR4-G, and (d) 12" COPR4-G. (*Source: NASA*) 39
3 CoPTR blades. (*Source: NASA*) 39
4 KA1Gen blades (a) without and (b) with 3.1 mil trip dots. (*Source: NASA*) 40
5 Example of collective angle adjustment using pitch block on CoPTR blades. (*Source: NASA*) 40
6 Test section of 14- by 22-Foot Subsonic Tunnel during VLPNT (looking upstream). (*Source: NASA*) 41
7 Planned points for (a) departure and (b) approach transition profiles for CoPTR blades. Note that symbol combinations are common across the three plots for each type of run conditions. 42
8 Speaker (indicated by arrows) mounted to PTS flange for reflection assessment (a) with and (b) without the fairing. (*Source: NASA*) . . 43
9 Schematics of (a) PTS dimensions (in inches) and (b) PTS internals. (*Source: NASA*) 44

10 Grid array of microphones. (*Source: NASA*) 45
11 Grid array microphone mounting (a) without and (b) with windscreens. Note grid caps were removed before installing windscreen. (*Source: NASA*) 46
12 Grid array microphone mounting for (a) upstream and (b) downstream three-microphone clusters. (*Source: NASA*) 46
13 North wall phased array. (*Source: NASA*) 47
14 Sample images of the laser scan results showing (a) the PTS relative to the phased array, (b) the phased array, and (c) the PTS flange. (*Source: NASA*) 48
15 Inflow speaker source (red arrow) in aerodynamic fairing (yellow box). (*Source: NASA*) 49
16 Propellor conventions for forces and moments. (*Source: NASA*) . . . 49
17 Load cell axis orientations based on PTS roll encoder setting, looking at PTS from test section inlet. (*Source: NASA*) 50
18 COPR5-L hover performance at M_{tip}=0.300 from VLPPT and VLPNT. 50
19 COPR5-L cruise performance from VLPPT and VLPNT. 50
20 COPR5-L edgewise conditions from VLPPT and VLPNT. 51
21 CoPTR hover performance at M_{tip}=0.300 51
22 Axial flight performance of CoPTR blades. 52
23 Different propeller and rotor efficiency metrics for CoPTR blades in edgewise conditions. 52
24 Different propeller and rotor metrics for (a) thrust and (b) power for the CoPTR blades in edgewise conditions. 53
25 Different propeller and rotor metrics for (a) normal and (b) side forces for the CoPTR blades in edgewise conditions. 54
26 Different propeller and rotor metrics for (a) yawing and (b) pitching moments for the CoPTR blades in edgewise conditions. 55
27 Different propeller metrics for efficiency for the CoPTR blades in edgewise conditions. 56
28 Potential rotor metric for efficiency for the CoPTR blades in edgewise conditions. 57
29 KA1Gen hover performance at M_{tip}=0.300. 57
30 KA1Gen cruise performance for different conditions. 58
31 KA1Gen edgewise conditions. 58
32 COPR2-G hover performance at M_{tip}=0.300 for different diameters. 59
33 COPR2-G cruise performance for different diameters. 59
34 COPR2-G edgewise conditions for different diameters, $\alpha_p = 45°$. . . 60
35 COPR4-G cruise performance for different diameters. 60
36 COPR4-G edgewise conditions for different diameters, $\alpha_p = 45°$. . . 61
37 COPR3-L hover performance at M_{tip}=0.300 for different boundary layer trip heights. 61
38 COPR3-L cruise performance without boundary layer tripping. . . . 62
39 Acoustic results from CoPTR in hover. Run 0581, $M_{tip} = 0.350$, $\beta' = 16°$. 62

40 Acoustic results from CoPTR in edgewise flight. Run 1005, $\beta' = 16°$, $\alpha_p = 88°$. 63
41 Periodic averaging results from CoPTR in hover. Run 0581, $M_{tip} = 0.350$, $\beta' = 16°$. 64
42 Periodic averaging results from CoPTR in edgewise flight. Run 1005, $\beta' = 16°$, $\alpha_p = 88°$. 65
43 Periodic averaging results from CoPTR in edgewise flight using the tachometer signal (left) and speaker waveform (right) as periods. Run 1075, $\beta' = 16°$, $\alpha_p = 80°$. 65
44 Contours of extracted broadband emissions for CoPTR blades in edgewise flight for $DL = 8$ psf and $M_\infty = 0.015$. 66
45 Examples of different beamforming techniques using the CoPTR blades. Run 1004, $\alpha_p = 88°$, DL = 8psf, $M_\infty = 0.015$. 67
46 Comparison of similarly-located microphones with and without windscreen cage, plotted in 64 Hz (left) and 512 Hz (right) narrowband bin widths. Hover Run 0581, $M_{tip} = 0.350$, $\beta' = 16°$. 68
47 Preliminary assessment of reflections off PTS aerodynamic fairing. . 69
48 Example of tested geometry (left) and as-designed geometry for data release (right). 70
49 Preliminary CAD geometry of full PTS and inflow speaker source as tested in VLPNT. 70

Acronyms and Nomenclature

Abbreviations and Acronyms

BPF	Blade Passage Frequency
$COPR$	Computationally-Optimized PropRotor
$CoPTR$	Commercial Prototype TiltRotor
DL	Disk loading, $T/(\pi R^2)$
GRC	NASA's Glenn Research Center
$KA1Gen$	Kinetic Analytics 1st Generation
$LaRC$	NASA's Langley Research Center
PTS	Propeller Test Stand
$RAVEN$	Research Aircraft for eVTOL Enabling techNologies
$VLPNT$	Vertical Lift Proprotor Noise Test
$VLPPT$	Vertical Lift Proprotor Performance Test

Dimensionless Quantities

c_0	Speed of sound, m/s
C_m	Pitching moment coefficient
C_n	Yawing moment coefficient
C_N	Normal force coefficient
C_P	Power coefficient
C_T	Thrust coefficient
C_Y	Side force coefficient

η	Propeller Efficiency
η_x	Propeller Axial efficiency
FM	Rotor figure of merit
J_p	Propeller advance ratio
J_{eff}	Effective propeller advance ratio
L/D	Rotor lift-to-drag ratio
M_∞	Tunnel Mach number, U_∞/c_0
M_{tip}	Tip Mach number, $\Omega R/c_0$

Symbols

α_p	Propeller pitch angle, degree
α_{TPP}	Rotor tip-path-plane angle, degree
β	Blade collective pitch angle, degree
β'	Collective angle at $r/R = 0.75$, degree
dB	decibels ref. 20 μPa
D	Proprotor diameter
f	Frequency, Hz
m	Pitching moment about y, Nm
n	Yawing moment about x, Nm
N	Normal force in $+x$, N
N_b	Number of blades
Ω	Rotation rate, rad/s
ψ	Azimuth angle, degree
$_p$	Propeller nomenclature subscript
Q	Torque, Nm
r	Radial position, m
$_r$	Rotor nomenclature subscript
R	Proprotor radius, $D/2$
ρ	Freestream density, kg/m^3
t	Time, seconds
θ	Elevation angle, degree
T	Thrust, N
U_∞	Freestream velocity, m/s
x	x-axis
y	y-axis
Y	Side force in $+y$, N
z	z-axis

1 Introduction

This report summarizes the design, execution, and resulting data from the Vertical Lift Proprotor Noise Test (VLPNT). This test was conducted in the NASA Langley Research Center's 14- by 22-Foot Subsonic Tunnel from July to December of 2025. Ten different blade configurations were tested at a variety of collective angle settings

and flow conditions, totaling over 4000 data points. Various measurement systems were utilized, including acoustic measurements taken by a microphone array in a grid pattern, a phased microphone array, dynamic load measurements from a six-axis load cell, and propulsor rotation rate using a laser tachometer.

2 Description of Test Articles

There were three primary focuses for VLPNT: 1) validate data collected during the Vertical Lift Proprotor Performance Test (VLPPT) [1] and capture acoustic data for the same conditions, 2) collect performance and acoustic data simultaneously across a wide range of realistic operating conditions for publicly-available geometries that are considered representative of real vehicles, and 3) perform a proprotor scaling study. An additional data set was also collected to investigate the effects of boundary layer tripping in hover. Four geometries were selected to achieve these goals: COPR-L, COPR-G, CoPTR, and prototype blades for the RAVEN vehicle (KA1Gen). These geometries are summarized in Table 1.

The Computationally-Optimized PropRotor (COPR) was developed by NASA as part of a pervious blade optimization effort [2]. Minor variations now exist due to differences in manufacturing processes, with the most notable difference being the tip shape. The blades manufactured for NASA's Langley Research Center (LaRC), which are referred to as COPR-L, taper to a narrow tip roughly centered on the blade quarter-chord line. Blades manufactured for NASA's Glenn Research Center (GRC), referred to as COPR-G, have a rounded leading edge and less taper, leading to a larger chord at the tip. The naming convention for these blade sets includes the number of blades, e.g., COPR5-L is a 5-bladed variant of the LaRC design and COPR4-G is the 4-bladed variant of the GRC design.

The first test objective was completed with a 2-foot diameter COPR5-L blade set, which was originally tested during VLPPT. These blades were fabricated from woven fiberglass and carbon fiber layers laid up over a polyurethane foam core with unidirectional carbon fiber spars reinforcing the leading and trailing edges. The surface was then painted. The same blades were used for the tripping data set, but in a 3-bladed configuration (COPR3-L). Images of the different COPR-L configurations are provided in Figure 1. The boundary layer tripping was performed via laser-cut adhesive vinyl dots, which had a diameter of 0.060" and were placed at 10% chord along the entire blade span, roughly 0.120" (two diameters) apart. The severity of the boundary layer disturbance roughly correlated with the "trip height", which was varied by having the dots cut from different thicknesses of vinyl. For this work, the trip heights varied between 3.1 and 9.9 mil (0.0031 to 0.0099 inches).

A set of blades originally made for the GRC Icing Research Tunnel were used for the scaling study. The blade sets were COPR4-G variants with diameters of 24", 28", and 36", all utilizing the same hub. These blades all consist of a combination of unidirectional and woven carbon fiber layers over a polyurethane foam core and were not painted. An additional COPR4-G set was fabricated from Formlabs Rigid 10k resin at 12" diameter scale. These blades thus provided a good opportunity for studying scaling relationships for proprotors. Sample images of configurations

utilizing each diameter are provided in Figure 2. The startup torque for the 36" COPR4-G blade set was prohibitively high given the current ramp-rate of the PTS, leading to the 36" diameter set only being tested in the COPR2-G configuration. Note that the 3 larger blade sets all utilized the same hub, meaning the root cutout was a larger percentage of the disk area as the diameter decreased. The 12" diameter set used a hub designed for that scale, so the root cutout for that blade set was closer proportionally to that of the 36" set.

Two blade sets were selected for the final test objective of collecting data for "realistic" blade geometries. The first blade geometry was developed by Joby Aviation in 2017 and the full-scale blades were used by one of the company's prototype flight vehicles. This geometry was then later made publicly available for use by the research community. Although the blade geometry was drastically altered for later iterations of flight vehicles, it is more representative of actually deployed geometries than many of the more 'canonical' shapes that are typical of research studies. These blades will be referred to by an in-house designation, the Commercial Prototype TiltRotor (CoPTR) blades, which were tested in a 2 foot diameter 5-bladed configuration, as shown in Figure 3. The second blade set were designed by Kinetic Analytics as a 3-bladed configuration as part of NASA's exercise in designing the RAVEN eVTOL vehicle. These blades, referred to as the KA1Gen blades, were also scaled to a 2 foot diameter for this test and are shown with and without boundary layer tripping in Figure 4. Both blade sets were injection molded from a nylon resin impregnated with long carbon fiber strands.

All blade geometries were tested in ground-adjustable hubs that allowed for testing multiple blade collective angles. Blade collectives were set using a Wixey WR300 Type 2 inclinometer. The inclinometer was placed on pitch blocks, which were custom designed and printed for each blade geometry. The pitch blocks were designed using the outer mold line of each blade geometry such that they rested on the upper surface of the blade (with the PTS pitched down and the proprotor tip path plane horizontal). A lip on the pitch block rested on the leading edge of the blade and the blade taper was utilized to properly locate the pitch blocks at the correct r/R radial location. The radial location of the collective angle setting for each blade geometry is summarized in Table 2, and an example of the inclinometer/pitch block is provided in Figure 5. Collective angle settings, β_{set}, were recorded in the run log and configuration code for each point, both of which will be described in more detail later. The set angle was the reading on the inclinometer. The collective angle convention of β' was introduced by Ref. [3] and is defined as the collective angle at a radial position of $r/R = 0.75$. The β'_{offset} in Table 2 allows for the calculation of β' based on the set angle recorded in the run log via $\beta' = \beta_{set} + \beta'_{offset}$. An additional pitch block was designed for the inverted CoPTR configuration that matched the outer mold line of the lower surface of the blades and rested on the trailing edge.

3 Description of Test

3.1 14- by 22-Foot Subsonic Tunnel

This test was conducted in the NASA Langley Research Center's 14- by 22-Foot Subsonic Tunnel (14x22). The 14x22 is a closed-circuit atmospheric tunnel that can be operated in closed- and open-jet configurations. The test section is 14.5 ft tall, 21.75 ft wide, and 50 ft long. The walls and ceiling are lifted out of the test section to achieve the open-jet configuration, leaving the floor in place. In this sense, the 14x22's "open-jet" configuration is better characterized as a quasi-open-jet. A collector at the downstream end of the test section is used to capture the expanded shear layer and direct the flow into the tunnel circuit. The open-jet configuration is typically used for acoustic tests in this tunnel, as was the case in this work. The tunnel can operate between Mach numbers of 0.02 and 0.26 in the open-jet configuration; however this test focused on Mach numbers of 0.16 and below. Flow speeds for this test were determined via a pitot-static probe located at the inlet of the test section.

A schematic of the full tunnel circuit can be found in Manuel et al. [4]; however the focus of Manuel et al. was to redesign the flow collector, so the schematic is not representative of the currently installed flow collector. Figure 6 includes an image of the test section set up for this test (looking upstream from the flow collector). The north wall of the test section (to the left in Figure 6) is treated with 6-inch melamine foam wedges, which have a nominal low pass cut-on frequency of 550 Hz. The ceiling, after being raised for the open-jet configuration, is also acoustically treated with the same wedges as the north wall. The south wall (to the right in Figure 6) consists of two types of acoustic treatment. The entire south wall of the test cell is treated with acoustic paneling, made up of fiber-cloth-wrapped fiberglass covered by perforated metal panels. Additional treatment was added to an upstream portion of the wall near the PTS location. This treatment included 2-foot fiberglass wedges suspended from a minimal extruded aluminum frame attached to points on the floor and wall such that there was a small air gap between the wedges and acoustic paneling. The wedges covered an area of 26 feet wide by 12 feet tall. The nominal low-pass cut-on frequency of the 2-foot fiberglass wedges are 140 Hz. Two floor carts make up 50 feet (25 feet each) of the floor in the streamwise direction, starting roughly 1 foot from the inlet of the test section (beneath and supporting the baskets, which are the bright white floor section in Figure 6). These carts were lowered 2 ft to allow for the placement of acoustic treatment in "baskets". The baskets used in this test used two densities of foam, 2 lb/ft^3 and 6 lb/ft^3, as fill material. The fill material was constrained on the sides by a coarse wire mesh. The top of the baskets had two components. Directly on top of the foam was a rigid wire grid of 1/4-inch diameter and 3-inch by 3-inch cells (i.e. 3-inch pitch). A 1/8-inch thick felt sheet (with an area density of 18 oz/yd^2) was stretched over the grid and fastened to the wire mesh on the sides of the baskets to minimize scrubbing noise. A previous iteration of the baskets used an adhesive-backed felt laid over the baskets, however, subsequent work showed that the adhesive backing was acoustically hard [5]. Six-inch thick cloth-covered fiberglass was installed on the floor in a wooden frame in the area between the baskets and the north and south walls to reduce floor reflections outside

of the core flow, with additional 4-inch fiberglass panels covering the exposed floor in front of the south wall wedge treatment. Six-inch thick polyurethane foam was used for the two downstream-most panels to avoid interactions between the cloth covering and the expanded shear layer. Previous tests used 4-in thick polyurethane foam glued to the floor to acoustically treat the out-of-flow floor area. The previous floor treatment was disposed of at the end of each test, whereas this treatment can be re-used in future entries.

3.2 Test Matrix

There were three main portions of testing, as described in earlier sections: repeating test conditions from the previous VLPPT entry, a proprotor scaling study, and a dataset of proprotors that are more practical for real-world use. The various combinations of data points are summarized for each blade set in Tables 3 - 6.

A subset of data points from VLPPT was collected for the COPR5-L blade set, including hover at three blade collective pitch angles, a sweep of cruise conditions, and a sweep of tunnel speeds and RPM at a 45 degree proprotor pitch angle. Note that, while the physical configuration in the global coordinate system was a yawing of the PTS, from the proprotor perspective these angle changes were treated as pitching configurations and will be referred to as such. The blade sets were also tested in hover at the 45 degree pitch configuration to investigate the effects of non-uniform inflow, since the PTS was facing the north wall instead of the center of the test section inlet. This configuration also directed the proprotor plane to be close to normal to the phased array, which will be discussed in Section 4.2.2.

The validation data set portion of the test included the CoPTR and KA1Gen blade sets. The CoPTR blades were tested in hover, cruise, and conditions meant to simulate take-off, approach, and descent. The planned departure and approach profiles are summarized in Figure 7. The KA1Gen blades were also tested in hover, cruise, and edgewise flight conditions, although the combination of these variables was reduced compared to CoPTR. Additionally, the KA1Gen blades were tested in hover and cruise with a boundary layer trip applied.

The scaling study utilized the COPR-G blade sets in two steps: COPR4-G (4-bladed configuration) and COPR2-G (2-bladed configuration). The COPR4-G configuration was used for the 12", 24", and 28" diameters, whereas the COPR2-G was tested with 12", 24", and 36" diameters. The COPR4-G blades were tested in hover, both aligned with the tunnel freestream direction and at a 45 degree pitch, a sweep of cruise conditions, and a smaller sweep of tunnel speeds and RPM at a 45 degree pitch. A more extensive data set was collected with the COPR2-G configuration, including the points collected with COPR4-G and additional blade collective angles in hover.

An additional data set was collected at the end of the test using the COPR3-L blade set. The COPR3-L blade set was included to collect data focused on airfoil self-noise. This data set consisted of capturing common advance ratios at different dimensional cruise settings and multiple boundary layer trip heights in hover.

Preliminary analysis of acoustic emissions during the test indicated the presence of reflections at lower frequencies. The aerodynamic fairing for the PTS was identified

as a possible source of these reflections, so additional data sets were collected in an attempt to isolate this effect. A small 3 inch speaker was mounted in a cylindrical housing on the PTS hub adapter, in the same location as the proprotor hubs. This speaker was pointed down at the PTS fairing and towards each wall. Microphone 36 from the downstream three-microphone cluster was disconnected and that channel was used by an additional microphone that was placed on a pole at approximately midpoint locations between the speaker and select microphones in the grid array. This process was repeated, with a reduced number of locations for the traveling microphone, with the PTS fairing removed. A comparison of the two PTS configurations is shown in Figure 8.

4 Instrumentation

The primary measurements collected during this test were focused on proprotor performance and acoustic emissions. The atmospheric conditions in the tunnel were recorded throughout, including test cell temperature, pressure, and relative humidity. These were used for the calculation of the speed of sound and nondimensionalizing performance metrics. Atmospheric data were sampled at lower frequencies, typically 10-50 samples per second, depending on the device. The freestream velocity was set based on Mach number.

4.1 Propeller Test Stand (PTS)

NASA's Propeller Test Stand (PTS) was used to mount and drive the proprotors. The PTS places the center of the rotor hub 83.5 inches above the test cell floor and allows for +/-90° of yawing motion of the proprotors. Note that the PTS yaw control was used to simulate pitching of the proprotor, similar to tilt-rotor vehicle operations. Therefore, physical yawing of the PTS will be discussed in this report as proprotor pitching, α_p. Also note that the lower portion of the PTS was shrouded in an aerodynamic fairing, which limited the PTS yaw range from 0° to -90° (counterclockwise) for this test. The proprotor/hub/motor assembly was mounted cantilevered from an ATI Industrial Automation© Mini 85 six-axis load cell, which will be discussed in more detail in Section 4.3. A Monarch laser tachometer was placed inside the nose cone of the PTS to provide a 1/rev measurement of the hub. The PTS operates as an open-loop system without an encoder, where the RPM setting on the PTS controller is based on motor feedback, so the laser tachometer output was used to determine the actual proprotor RPM. A 7/0 AWG wire was wrapped around the vertical strut of the PTS to minimize vortex shedding. A dimensioned schematic of a portion of the PTS (without the wire wrap) and a section view of the PTS internals are shown for reference in Figure 9. The assembly shown in the section view of Figure 9 mounts to a roll motor, which was used to control the orientation of the x and y axes of the load cell, which will be discussed later.

4.2 Microphone Instrumentation

Two microphone arrays were utilized during the test. Microphones were placed on the south wall of the test section (right side in Figure 6) in a grid pattern. Additionally a phased array was located outside of the flow near the inlet on the north side of the test section (left side of Figure 6). Details on each array are in the following sections.

Data were collected using a National Instruments© PXIe-1085 chassis. The internal clock for the chassis was set using a PXIe-6674T timing card and time stamps were generated via IRIG-B [6] using a PXI-6683H card. The microphones in the phased array were sampled using PXIe-4499 acquisition cards and the south wall grid array microphones using PXIe-4480 acquisition cards. The center microphone of the phased array was sampled by both sets of cards. All channels were sampled at 131,072 samples per second, with the exception of a subset of points with the 12" diameter blades, where the grid array was sampled at 262,144 samples per second. A synchronization pulse was generated at 1 Hz by a Keysight© 33220A arbitrary waveform generator and was sampled by both sets of acquisition cards. The tachometer signal and any output waveforms sent to speakers, discussed later, were recorded by both sets of acquisition cards.

4.2.1 Grid Array

A grid array of stationary microphones was placed on the south wall of the test section. This was done to provide results similar to previous entries that utilized a traversing vertical tower of microphones without needing to traverse the microphones in the streamwise direction. The array consisted of 30 Brüel and Kjær© (B&K) 4939 microphones, powered using B&K 5939L power supplies, forming a grid pattern three microphones tall and 10 microphones in the streamwise direction. The three microphones in each vertical column were placed such that the middle row aligned with the center of the PTS hub (83.5 inches above the floor). The additional rows were placed ≈45 inches above and below the center row to capture acoustic emissions at ±10 degree azimuthal angles with respect to the proprotor. The array had one column of microphones in line with the rotor plane (when $\alpha_p = 0°$), which aligned the center microphone of this column with the PTS hub (microphones 2, 12, and 22). The additional columns were split, with one column 48 inches upstream (10.25 degrees above the blade plane) and 8 columns downstream at 2-foot ($\approx 5°$) intervals. An image of the grid array with dimensions and observer angles (when α_p=0°) is provided in Figure 10. Note that the observer angles are defined as elevation in the streamwise direction and azimuth in the vertical direction, following the convention of a traditional rotor in hover, such that the test section inlet is directly above the vehicle. The south wall treatment behind the grid array placed the wedge tips 272 inches from the tunnel centerline. Microphones were placed at the end of 1/4-inch diameter tubes, 12 inches long, which were mounted to a wire mesh that spanned the tips of the acoustic wedges. Adapters were printed from photoresin to hold the microphones in place at the end of the tubes. The combination of the tube and adapter placed the plane of the microphone diaphragms 256 inches from the tunnel centerline, with the exception of the first column (microphones 1, 11, and 21), which

were an additional 9.5 inches further away. The printed adapters incorporated a 'cage' consisting of four 0.1-inch diameter arms, over which 2 layers of thin nylon material were stretched [7]. This mounting configuration can be seen with and without the nylon material in Figure 11. This nylon acted as a wind screen, isolating the microphones from any hydrodynamic pressure. Specifically, a pressure wave is known to move through the wind tunnel circuit roughly every 10 seconds [8]. This phenomenon is not unique to the 14x22 and is common in closed-circuit open-jet wind tunnels. However, it has been observed to be exacerbated in semi-open-jet configurations where the floor is left in place [9, 10]. The azimuth and elevation angles for each microphone were used to determine a total incidence angle relative to the PTS hub, which could then be used to correct for incidence angle effects at higher frequencies as per the manufacturer. Note that the grid caps for the grid array microphones were removed before the nylon wind screens were installed.

Two additional sets of microphones were placed on the south wall to investigate the use of the 'three-microphone' method [11]. This method utilizes three closely-spaced microphones to attempt to filter out flow noise. The clusters were placed 61 inches above the floor (-5° azimuth angle), with one in-line with the PTS hub in the streamwise direction and the other 149 inches (30 degrees) downstream. These microphones are shown in Figure 10 as numbers 31-36. The microphone holders in the upstream cluster were in the tip path plane, Figure 12a, whereas the downstream cluster had angled tips to point the microphones at the PTS hub, as shown in Figure 12b, so incidence angle corrections were not required for these microphones. These microphones were not outfitted with windscreens and so the protective grid caps were left in place for the duration of the test.

4.2.2 Phased Array

A phased microphone array was placed in front of the north wall of the test section, and positioned sufficiently far upstream as to be out of the shear layer. The array was comprised of 54 B&K Type 4958 1/4-inch microphones. The innermost 45 elements were arranged in nine arms of five microphones and utilized a reverse-log distribution [12]. This array layout was chosen to minimize the 3-dB beamwidth while maintaining peak sidelobe levels at least 10 dB below the main lobe over a range of 1 to 16 kHz. Additionally, an outer ring of nine microphones at a diameter of 48 inches was added to improve low frequency resolution. The microphone pattern can be seen in Figure 13a. The phased array microphones were mounted to 18 inch metal tubes via printed adapters such that the microphone diaphragms were ≈20 inches from the support structure. The structure of the array back plate is a minimalist frame milled out of aluminum to minimize the amount of reflective surface directly behind the microphones. Additionally, 8-inch open-cell foam wedges were fixed to the support structure to damp remaining acoustic reflections. The microphone-frame-wedge configuration can be seen in Figure 13b. Additional information on the phased array can be found in Ref. [13]. There was also a B&K Type 4954 microphone placed in the center of the array to be used as reference, which was not included in beamforming calculations. This reference microphone was sampled as the final microphone channel in both the phased array and the grid array. The diaphragm

of the reference microphone is considered the origin when discussing locations of other test object and tunnel features relative to the phased array. The test section was laser scanned, with reflective spheres placed over the phased array microphones. Images of the laser scan point cloud are provided in Figure 14 for reference. The data from the laser scan were processed to tabulate the as-tested positions of the phased array microphones and the PTS, which are provided in Table 7. Note that, as shown in Figure 14c, there was no hub mounted on the PTS during the scan, so the PTS location in the table is the center of the face of the PTS flange. The distance between the flange face and the proprotor tip path plane needs to be extracted from the released geometries and accounted for. Also, note that the PTS was at $\alpha_p = 0°$ during the scan, so the yawing of the PTS must also be geometrically taken into account for any case where $\alpha_p \neq 0°$. The distance between the center of rotation for the yaw stage of the PTS and the PTS flange face is 16.48 inches.

An inflow noise source was used to produce specific waveforms to allow for the assessment of the impact of the shear layer on the signal reaching the phased array. The source was a 2-inch Dayton Audio© DMS58 speaker which has a working range from 160 Hz to 20 kHz and was embedded into a streamlined elliptical fairing, measuring 21 inches in the streamwise direction. The speaker-fairing assembly, shown in Figure 15, was supported by an aluminum 8020 post covered by a NACA 0024 airfoil with a 16-inch chord. The speaker was placed such that the diaphragm was 30 inches downstream, 40.2 inches below, and 169.4 inches in front of the phased array reference microphone. Three types of waveforms were used during this test, with the characteristics and frequency bounds for each provided in Table 8. The waveforms were generated in MATLAB and exported as *.wav* files to the data acquisition system. The white noise and "multisine" signals are described in Ref. [8]. An additional waveform was used for this test, a modulated tone centered at 3 kHz. This waveform was designed to allow for time-domain assessments of the shear layer. Output waveforms were generated via an NI PXIe-6124 and sent through a Crown Macro-Tech 600 amplifier. The commanded waveform was recorded as a direct output from the signal generator prior to run 3001, after which the commanded waveform was recorded as the output of the amplifier divided by 20. This change was made to capture any effects that the amplifier could have on the waveform.

4.3 Load Measurements

Load measurements were collected using an ATI Industrial Automation© Mini-85 load cell and recorded with a National Instruments© PXIe-4499 acquisition card. The largest calibration range was used to accommodate the preload created by the mounting of the motor and hub assemblies. The limits of this range are 420 lbf in x and y, 840 lbf in z, and 740 in-lbf moment in all three directions. For this test, the $+z$ of the load cell was typically in the direction of thrust (opposite the freestream), whereas $+x$ and $+y$ were functions of the commanded PTS roll angle. The PTS roll motor was commanded to different angles depending on the test condition to either avoid unnecessarily large preloads on individual load cell axes or to maximize the possible side loading conditions during test cases where the proprotor was pitched. The roll angle was held steady during run sequences and recorded. The rotations

from load cell coordinates to proprotor coordinates (i.e. x, y, z to T, N, Y) are provided later.

Static pull tests were performed before and after the test to verify the health of the load cell. Loads were applied purely in the -z-direction via a pulley and straight down to capture side loading and moments. Thermal soaks were performed at the start of each run sequence to mitigate the effects of thermal drift on the load cell. The PTS was brought to a mid-range RPM for the mounted proprotor and that RPM was held until the measured thrust stabilized. These thermal soaks were performed in a static test cell for hover run sequences and with the wind tunnel at a Mach number of 0.03 (≈10 m/s) for all other conditions. Once the thrust reading was stable, the PTS and tunnel, if applicable, were brought to rest and a wind-off zero (WoZ) point was taken to act as a tare. Selected test points were repeated throughout the run sequence to monitor the thermal drift of the load cell, and a second WoZ point was collected at the end of the run sequence. The drift in the load cell measurements throughout the run sequence, calculated as a difference in WoZs, was used as part of the uncertainty calculations. The difference in WoZs was less than one pound in F_z, and typically below 0.2 pounds.

The data in this report are provided as force and moment coefficients, as defined Table 9. Note that the coefficients are typically calculated using propeller conventions, however rotor conventions are used where appropriate and conversions between the two nomenclature are included in Table 9. The dimensional loads are also available as part of the data release. The conventions used for performance data in this test are cataloged in Figure 16. Three different PTS roll angles were used throughout the test, and the load cell orientations relative to the proprotor schematic are provided in Figure 17.

Uncertainties were calculated for force coefficients, moment coefficients, and dimensionless efficiency parameters using the method described in Figliola and Beasley [14]. The uncertainty analysis included the values measured by the load cell, the tachometer signal, and air density. The air density used in the determination of the coefficients was the humid air density, which was calculated using ambient temperature, ambient pressure, and the dew point temperature. Random and bias errors in the humid air density were calculated using the same method. Bias errors for the tachometer signal and atmospheric measurements were taken from the data sheets for the respective measurement devices. Bias errors for the load cell measurements were a combination of the measurement resolution for each axis and the drift between pre- and post-sequence WoZ measurements. The random errors were calculated as the standard deviation of the measurement divided by the square root of the number of data points. The total number of points was used for the tachometer signal and atmospheric measurements, and the number of revolutions was used for the load cell measurements. Bias and random errors due to the diameter of the proprotors was neglected.

5 Results

This section presents a set of preliminary data from the VLPNT entry. Given that this report serves as a description of the test and a release of the data, the analysis presented herein is limited. Select performance and acoustic data will be provided, along with discussions about how to properly handle the data. This includes a discussion on propeller versus rotor nomenclature for performance data and the different corrections that should be applied to properly analyze the acoustic data.

5.1 Performance Data

Samples of performance data from the different blade sets are provided in this section. The data are presented in dimensionless parameters and with error bars representing uncertainties, which were calculated as described in Section 4.3.

5.1.1 Validation of COPR5-L Data from VLPPT

As mentioned previously, the first blade set tested was a duplicate of one of the blade sets from the previous Vertical Lift Proprotor Performance Test (VLPPT). Figure 18 compares the hover condition from VLPPT to a set of hover conditions at different blade collectives from the current entry. The thrust and power coefficients at $\beta' \approx 17.5°$ differ by roughly 15%, however the figure of merit for the two cases align well. The discrepancies could be due to the blade collective setting, since the process for accurately setting the collective angle has been refined since the VLPPT entry; however, the figure of merit agreement is encouraging.

A similarly encouraging agreement is shown in the plots in Figure 19, which compare the advance ratio sweep in cruise (i.e. pure axial flight). Note that smaller advance ratios indicate low tunnel speeds and high proprotor RPM. This is the worst-case combination for thermal drift of the load cell, which is likely why the error bars are larger at smaller values of J_P. The data agree very well between the two tests. The power coefficient curve from VLPPT exhibits a hysteresis-like trend at lower advance ratios, which is not present in the VLPNT data. A more in-depth analysis of specific run conditions during the two tests could shed light on this trend.

The edgewise flow conditions, shown in Figure 20, also show good agreement between the tests. Note that a larger range of α_p was tested during VLPPT. Also, the trends across different pitch angle cases nicely collapse when plotted against J_{eff}, which is likely the more appropriate variable to consider for this case; however, the trends are shown plotted against J_P to allow for differentiation between pitch angle cases to better show the agreement between the two data sets.

5.1.2 Large-envelope Validation Data Set

The performance data from the "realistic" blade sets will be discussed next. The CoPTR blade set was tested under a wide variety of operating conditions. A baseline hover data set was first collected. The performance data from a limited collective sweep in hover are shown in Figure 21. The roughly flat figure of merit curve for the tested collective range is consistent with trends observed by other research groups

using a larger scaled version of this blade design [15], [16]. An advance ratio sweep of these blades in cruise is provided in Figure 22, with a peak axial efficiency of approximately 0.81 occurring at an advance ratio of $J_P = 1.1$. Additional data are included in these figures, which show the pure climb and descent performance of the blades at a nominal hover collective ($\beta' = 16°$). The pure descent cases are likely good candidates for further study since simple momentum calculations indicate vortex ring state was likely during some conditions. Extreme unsteadiness was observed in the load cell data during the collection of these points, and as such the load data released for the pure descent conditions will include time histories of performance data instead of mean values for each run condition.

As shown in Figure 7, these blades operated over a range of operating conditions meant to simulate departure and approaching transitional flight for a tiltrotor vehicle. This has created questions about proper terminology and nomenclature for these operations. This report has focused on utilizing propeller nomenclature for performance metrics and other values such as advance ratios (J_P and J_{eff}), with the exception of hover efficiency, where rotor figure of merit is intuitively the correct metric. Figure 23 compares different performance metrics for efficiency in propeller and rotor nomenclatures. Left to right, these are propeller efficiency ($\eta = (J * C_{T,p})/C_{P,p}$), propeller axial efficiency ($\eta_x = J * (C_{T,p} cos\alpha_P - C_{N,p} sin\alpha_P)/C_{P,p}$), the axial component of propeller efficiency ($\eta * cos(\alpha_P)$), and rotor lift-to-drag ratio ($L/D = (\mu C_{T,r})/C_{P,r}$). Propeller efficiency is an obvious metric for axial flight, and has been used up to this point in this report. Propeller axial efficiency includes the axial component of thrust and accounts for normal forces ($C_{N,p}$). Both efficiency and axial efficiency provide non-physical results for many of the tested conditions, with efficiencies as high as 4 and negative axial efficiencies. These are due to the complete neglecting of the normal force for the former and the normal forces dominating the thrust for the latter. The axial component of efficiency (essentially axial efficiency with the normal force component removed) was also investigated as a potential solution to this problem, but the derivation is less rooted in physics and the results still exceed 1. This effort indicated that, at least for some range of pitch angles, propeller nomenclature is no longer valid. The rotor lift-to-drag ratio effectively serves as a forward flight efficiency metric for rotorcraft, and was therefore identified as a possible alternative metric for these flight conditions. Note that the pitch angle conventions between rotor and propeller nomenclatures are referenced to normal planes, such that $cos(\alpha_{TPP}) = sin(\alpha_P)$. Interestingly, the trends in the L/D data are very similar to the propeller efficiency, but with the added benefit that $L/D = 4$ is not non-physical. The data appear to roughly collapse to three linear trend lines; however, different collectives do not necessarily all fall onto the same trend line. Future investigation into local flow regimes across the blade span at different collectives and flight conditions could explain the different trends. Unfortunately, although L/D appears to handle the transitional region better than propeller nomenclature, it cannot be the sole solution, since by definition both μ and therefore L/D are zero for pure axial flight.

While efficiency is a useful tool for demonstrating some challenges of determining appropriate nomenclature, other parameters are need to fully describe transitional operations. Figures 24 through 28 provide all of the performance metrics in propeller

and rotor nomenclature. Thrust and power coefficients (Figure 24) do not obviously collapse using any combination of metrics, whereas side forces and moments could arguably be said to collapse using both propeller and rotor nomenclature. This report is not intended to determine which parameters are best to use in each operation; however, it does provide a broad data set that could be useful in making these determinations. Performance metrics in the remainder of this report for edgewise conditions will include both propeller and rotor efficiencies.

A second data set was also collected to interrogate different flight conditions using the KA1Gen blade design. Figure 29 provides hover performance data, including one condition where a boundary layer trip (trip dots) was applied. The 3 mil tall boundary layer trip dots were also applied for a cruise sweep, shown in Figure 30. The boundary layer tripping appeared to provide a slight reduction in required power and therefore a small increase in efficiency in both hover and cruise. The blades were also tested at a second, higher collective during cruise, which shifted the efficiency curve up in advance ratio, but did not increase the peak efficiency. Finally, two transition configurations were tested, shown in Figure 31. These conditions were selected based on internal performance modeling for the full-scale RAVEN vehicle.

5.1.3 Proprotor Scaling Study

The scaling study was performed in two portions, with 2-bladed and 4-bladed configurations of COPR-G, as described earlier. A collective angle sweep was performed for the 2-bladed configuration, which included 12", 24", and 36" diameter proprotors, as shown in Figure 32. The three diameters demonstrated very similar power curves, however the 24" diameter blade set underperformed in thrust, and therefore figure of merit. This is likely due to the increased root cut out percentage for the 24" diameter set, since the 24", 28", and 36" diameters all utilized the same hub. The 12" diameter agreed better with the 36", since it used a unique, smaller hub. The error bars for the smallest diameter are notable larger, which is expected given the extremely small loads generated by the 12" diameter COPR2-G proprotor. The largest dimensional thrust recorded for the 12" blades in hover was approximately 5.3 lbf, whereas the load cell range was ± 840 lbf with a resolution of ± 0.094 lbf. Performance data at the 12" scale is still valuable, however, especially since it could be compared against or augmented with data from other facilities with more appropriately sized test stands. The cruise data for the COPR2-G configurations, Figure 33, show similar trends. This includes all three diameters having good agreement in required power, with the 24" diameter underperforming in thrust and therefore efficiency. The trends shown during the edgewise flight conditions ($\alpha_P = 45°$, Figure 34) are more difficult to parse. The 24" diameter underperforms the 36" in all metrics. The 12" diameter proprotor had large errors, but trended decently well with the 36" in axial efficiency.

The maximum diameter for the 4-bladed configuration, COPR4-G, was reduced to 28 inches to accommodate the maximum startup torque of the PTS. This configuration was only tested at one collective in hover, so that data are not plotted. There is better agreement between the three diameters at the cruising conditions shown in Figure 35. This is likely due to the root cutout percentage being more similar for the

24" and 28" diameters than in the 2-bladed configuration, along with the 4-bladed configuration generating larger dimensional loads for the 12" diameter proprotor. Interestingly, the performance curves for the edgewise conditions, Figure 36, do not show an inherently obvious trend in performance based on diameter, with the 12" diameter generally having the best efficiencies, then the 28" diameter, with the 24" having the lowest. A possible explanation is that the root cutout percentage has an increased impact on edgewise performance, and the efficiency decreases as that percentage increases. This could be interpreted to agree with the trends observed in the COPR2-G data.

5.1.4 Airfoil Self Noise Data Set

The COPR-L blade geometry was also tested in the COPR3-L configuration to study airfoil self noise mechanisms as data of opportunity. These tests included a hover collective sweep with different boundary layer trip heights, Figure 37, and a set of data points in axial flight, Figure 38. The boundary layer trips were applied in three heights, 3.1, 6, and 9.9 mils. Boundary layer tripping did not appear to have an effect on the performance of the proprotor. It is possible that the slightly decreased performance at $\beta' = 12^\circ$ for the 9.9 mil trip height indicates over-tripping; however, it is difficult to be conclusive given the error values. Analysis of the acoustic data may be more enlightening. The intention of the cruise conditions was to collect specific advance ratios with different combinations of dimensional conditions (i.e. different combinations of tunnel and tip Mach numbers that led to the same J_P). The performance data also show good agreement when plotted against J_P, reinforcing the value of the metric in proprotor analysis.

5.2 Acoustic Data

A fundamental objective of this test effort was to measure acoustic emissions. However, acoustic data are less straightforward to process and correctly interpret than performance data. Therefore, this report will not include a large repository of acoustic results the way the performance data were presented. Instead, this section is meant to provide all necessary information for the data to be successfully utilized by the community, as well as a limited set of examples.

5.2.1 Data Corrections

Certain decisions were made during the experimental design and set up that necessitate special care when interrogating the acoustic data. This includes a variety of corrections that must be applied to the data. Depending on the microphone, corrections may be required to account for the presence of the protective grid cap, source incidence angle, and atmospheric attenuation. Corrections for the protective grid cap and incidence angle are from the microphone manufacturer and are model-specific. Atmospheric attenuation should be accounted for since the test period spanned from August to December, covering a wide range of temperature and humidity in the test cell, and because of the size of the test section, with microphones being in the range of 20 to 40 feet from the source. A guide for the application of the corrections is

provided in Table 10. Additional corrections may be prudent, depending on the data analysis, such as correcting levels to a common radial distance from the source.

Figures 39 and 40 provide examples for the application of the corrections for a hover and an edgewise case. These examples demonstrate the value of the proper application of corrections. The raw spectra from the hover condition, Figure 39c, could be interpreted to mean that there was a directivity component to the higher-frequency content for that case, with microphone 12 being ≈2 dB above microphone 20. However, the corrections accounting for the angular and distance differences between the microphones relative to the source show that this is not the case, as seen in Figure 39d. Conversely, applying the corrections to the edgewise case, Figure 40c,d, confirms the directivity of the source. Unfortunately, care must still be taken to properly apply the corrections. Note the roll-up in the spectra of microphone 20 beginning at approximately 40 kHz, seen in Figures 39b and 40b for the hover and edgewise conditions, respectively. This is likely due to the greater distance of that microphone from the source than microphone 12, such that the calculated atmospheric attenuation correction is greater in magnitude. If the acoustic signal is below the noise floor for a given channel, then the atmospheric attenuation correction will begin to artificially increase the noise floor. A potential solution for this is detailed in Ref. [17] where the background noise measurements were used to systematically determine a threshold where atmospheric attenuation corrections were unreliable and therefore no longer applied.

5.2.2 Periodic Averaging

A valuable tool for proprotor acoustic measurements has been periodic averaging. This method takes the pressure time history from one microphone and divides it into sections based on a user-defined period. These sections of time can then be averaged, emphasizing aspects of the signal that repeat across instances of the period and suppressing aspects that are not. This allows for the isolation of the frequency characteristics of the selected period. This method was described in detail using a speaker and known waveforms in Ref. [8]. In the case of the speaker noise source, the waveforms had a known period of 0.5 seconds, and non-periodic content was assumed to be stochastic background noise. When applied to a proprotor, a 1/rev signal like that generated by a laser tachometer can be used to define the period, and the non-periodic content includes both stochastic background noise and the non-periodic emissions of the propulsor (also known as "broadband" noise). Examples of periodic averaging based on the revolution speed of the proprotor are provided in Figures 41a, 41b, 42a, and 42b, for hover and edgewise conditions, respectively. An additional step that may be useful, depending on the characteristics of the acoustic emissions, is removing the peaks from the broadband content to better visualize the "broadband shelf". This can be done with a simple peak-finding routine, which was the method used here, or an averaging function like a moving bandwith filter. The broadband content with the peaks removed is also provided in the example figures. Figures 41c and 41d demonstrates how peak removal can be useful to more clearly visualize the directivity of the broadband noise, whereas the visualization of the broadband content in Figures 42c and 42d is not aided by removing the peaks.

The period used for averaging can be selected to isolate different signals. This can be demonstrated by looking at a run condition where an inflow speaker was present, mounted in an aerodynamic fairing upstream of the PTS as shown in Figure 15. Figure 43 shows acoustic emissions from a case where the CoPTR blades were in an edgewise flight condition with the inflow speaker source simultaneously outputting a known waveform. Periodic averaging could then be applied using the tachometer signal to isolate the periodic and broadband emissions of the proprotor, shown on the left side of the figure. Since the speaker was simultaneously outputting a waveform with a known period, the microphone data could then also be periodically averaged using the period of the speaker waveform. The extracted speaker signal is shown in the right side of the figure, along with the isolated speaker output, measured without the blades spinning and the tunnel flow off. Note how periodic averaging was able to capture the speaker output even though the background flow noise of the tunnel and the acoustic emissions from the blades were generally 10 dB or greater than the speaker output.

Periodic averaging must be done carefully. The application of this method to speaker data is fairly simple, since the noise source has a known and constant period. The period of proprotors is less exact, with the motor RPM varying slightly in time. This can present as an inconsistent number of samples per revolution. A few different methods for how to handle this are available. The method used to generate the results in this report determines the most common number of samples per revolution and uses that value as a fixed period. This method assumes that the number of samples per revolution follows a roughly Gaussian distribution, such that the occurrences of larger and smaller numbers of samples per revolution are symmetric yet uncommon enough to be negligible. Alternative methods include modifying the previous method to discard any revolutions whose samples per revolution are outside a threshold centered on the mode value, such as the mode number of samples per revolution ± 2. Other potential methods include interpolating each revolution to match the most common number of samples per revolution or finding the minimum number of samples per revolution and interpolating all revolutions down to that value to avoid upsampling. The "ideal" method for handling RPM variations has not been investigated, and such an investigation would need to include edge cases to be conclusive.

5.2.3 Grid Array

The grid array was designed with two advantages in mind. The first was to provide the ability to capture a reasonably large area of emission directivity. This could be done with a single linear array via a tower of microphones to create a single vertical slice of directivity, as was done in past tests [8, 18]. However, the linear array method would require the tower to be traversed along the length of the test section, with a data point at each desired streamwise position. This method is time-intensive, and would be more difficult for a proprotor test where the motor temperature could effect performance data compared to previous tests focused on airframe noise or acoustic characterizations. This then leads to the second design advantage of the grid array in that the entire desired area of directivity can be captured in a single data point.

The grid array therefore removes the need to assume that multiple points with a traversing linear array are capturing identical test conditions.

Although an ideal grid array would allow for the capture of an entire hemisphere, similar to the ground-based snapshot arrays utilized in recent flight tests [17], time, resource, and physical constraints in the test cell constrained the size of grid array deployed for this test. Nevertheless, instantaneous directivity measurements from the grid array are still valuable. An example of using the grid array to create emissions contours is provided in Figure 44. The figure shows the broadband directivity under the CoPTR blades at different edgewise conditions for a constant disk loading of 8 psf and tunnel Mach number of 0.015. The contoured acoustic data shown are the extracted broadband content after periodically averaging each microphone pressure time history based on the 1/rev tachometer signal. The data were also frequency-scaled from the 2-foot diameter test article to a 10-foot diameter proprotor to be more representative of a real vehicle, based on the linear relationship between diameter and rotation speed to maintain a tip Mach number. Lastly, the data were A-weighted and normalized to a distance of 10 "full-scale" rotor radii from the source, before calculating the Overall Sound Pressure Level (OASPL) at each microphone. The flow in these figures is moving from left to right. Note that the azimuth and elevation angles provided in the figures are constant for all α_p and relative to the source location when in axial flight ($alpha_p = 0$), as opposed to the more conventional rotorcraft reference frame where 0° is the horizon and -90° is beneath the vehicle.

5.2.4 Phased Array

The 54-channel phased array was included both as a means of determining source locations in the test cell and improving signal-to-noise ratio. A variety of array processing techniques were applied including conventional frequency domain beamforming (CFDBF), CLEAN, DAMAS [19] and rotating source identifier (ROSI) [20]. In-house codes were used to perform CFDBF and subsequently apply the post-processing method DAMAS to improve resolution. Similarly, the beamforming software AVEC [21] was leveraged to first perform CFDBF and then to apply the post-processing method CLEAN to improve spatial resolution of the beammaps. Finally, the rotation tracking method ROSI was applied. ROSI calculations are carried out in the time domain rather than the frequency domain, and as such there are currently no known methods to improve spatial resolution. Beamforming results included in this report serve as qualitative examples using the data collected during this test. More details on the beamforming methods will be provided when results are finalized and published.

Illustrative results are provided in Figure 45 for the CoPTR blades in edgewise flight with a tunnel freestream flow of Mach 0.015 and an advance ratio of 0.046. The frequency band depicted is a one-third octave band centered on 8 kHz. The CoPTR blade geometry is depicted in Figure 45a where $\alpha_p = 88^\circ$. Figures 45b and 45c show the CFDBF results using the in-house code and AVEC, respectively. Figures 45d and 45e show the results of DAMAS and CLEAN, respectively, applied to the results presented in Figures 45b and 45c, respectively. Finally, the results of the derotational scheme ROSI are depicted in Figure 45f. Note that the results

shown are intended to represent the possible beamforming methods that may be applied to the data and should not be taken as quantitatively accurate. At time of writing, the in-house processing codes were still in the process of being adapted to the test data, and a thorough validation is underway and will be published later.

5.2.5 Additional Observations

Preliminary analysis of the data during the test identified two sources of reflections inherent to the experimental design. First was the wind screen cages used on the microphones in the grid array [7]. Small ripples were observed in the broadband hump, starting at approximately 10 kHz. This is believed to be due to the thin structure of the cage in front of the microphones. Data were compared between two similarly-located microphones with and without a wind screen to confirm this. Figure 46 compares microphones 12 (centered on the PTS hub) and microphone 31 (centered on the PTS hub in the streamwise direction and 5° below microphone 12), where microphone 12 had a windscreen and microphone 31 did not. The correction was applied to microphone 31 to remove the influence of the protective grid cap, and the resulting spectra were compared for the CoPTR blades during a hover condition. A slight ripple of roughly ± 0.5 dB can be observed in the data from microphone 12 compared to microphone 31 above $\approx$10 kHz. Although this reflection is unfortunate, data from the previous acoustic characterization of the 14x22 showed significant low-frequency corruption due to the hydrodynamic pressure wave that travels the tunnel circuit [8]. Given the rotation speeds of the test articles in this entry and the resulting frequency range of the BPF, it was determined that the windscreen cage reflections were preferable.

The second intuitive source of reflections was the aerodynamic fairing covering the base of the PTS. The design of the PTS requires a large fairing to cover the base, which means a hard surface that is rounded for aerodynamics and therefore a complex scattering body. A simple test was conducted in an attempt to assess the reflections from the fairing. A small 3 inch speaker was mounted to the PTS flange in place of a proprotor hub, as shown in Figure 8, and waveforms were sent to the speaker with it pointing down at the fairing, towards the grid array, and towards the phased array. Figure 47a compares transfer functions between the pressure time history recorded by microphone 12 and the waveform sent to the speaker. The dashed lines in the figure bound the region where there appear to be significant reflections coming from the fairing, roughly between 3 and 11.5 kHz. Figure 47b shows a comparison of the CoPTR blades in a hover condition with and without the fairing, with the left side comparing the entire frequency range and the right side focused on the range that fairing reflections appear to be present.

6 Data Availability

Data from this test are available in two ways. A subset of run conditions will be hosted online. These runs are summarized in Table 11. A reduced run log and the relevant blade geometries will also be hosted. The complete data set will be available electronically upon requests made to the authors. Requests for access

to either the complete data set or the online subset should be directed to Colin Stutz (colin.m.stutz@nasa.gov) or Nikolas Zawodny (nikolas.s.zawodny@nasa.gov), NASA Langley, Mail Stop 461, NASA Langley Research Center, 23681. Detailed information on data files and blade geometries are provided below. Microphone positions with respect to the proprotor hub are also available. A spreadsheet logging each data point and documenting the run conditions is also available, which will be required to parse the data files. The released run log includes date, run number, configuration and condition codes, and any recorded notes. The configuration code is a 10-digit numeric code that describes the configuration of each run sequence (i.e. parameters that were held constant during the run sequence, such as blade collective angle). The condition code is a 15-digit alphanumeric code that describes the specific test conditions of each point. The run log file includes sheets providing definitions for the configuration and condition codes. The run log begins at run 86 and ends at run 4076. Data points before run 86 were collected during test set-up and tear down for various reasons, such as verifying the acquisition system set-up and checking the health of the load cell after model transit, and although those points were retained internally they are not part of the data release.

6.1 Data Files

Three .mat data files were created for each point: 1) pressure time histories from the grid array microphones, 2) pressure time histories from the phased array microphones, and 3) processed load cell data. The tachometer signal and a time sync pulse are included in the microphone and load cell data files as additional columns to allow for periodic averaging and syncing the different files. The variables included in each file are provided in Tables 12 through 14 for microphone and load data. File names are all formatted as *'T686Rx_y.mat'*, where *'x'* is the run number and *'y'* is *'GridArray'*, *'PhasedArray'*, or *'LoadData'*, depending on the contents.

Microphone pressure time histories were recorded as raw binary files, which were converted during data reduction to Pascals. The conversion accounted for the A/D conversion, any gain applied to the channel, and used the most recent recorded sensitivity for each microphone. Sensitivities were determined using a B&K Type 4228 pistonphone and were re-recorded whenever the microphones were de-energized or re-energized. The commanded waveform to the inflow speaker source is also included in the microphone files. This channel was recorded for every run, regardless of whether or not a waveform was generated, so for most runs it captured the channel noise floor.

The commanded waveform was recorded as a direct output from the signal generator prior to run 3001, and after that run the commanded waveform was recorded as the output of the amplifier divided by 20. This change was made to capture any effects that the amplifier could have on the waveform. A notes variable is included in each data file, which includes some useful information on the units in the file and the date it was reduced.

Processed load data files typically contain data averaged over the point. This includes dimensional forces and moments in the load cell frame of reference and dimensional force and moment coefficients in propeller nomenclature (i.e. F_x, F_y,

etc vs. N, Y, etc). Figure of merit (helicopter nomenclature applicable to hover conditions) is also included. Note that the propeller efficiency term, called *'eta'* in these files, is actually η_x, which simplifies to η when the PTS was at 0° yaw and accounts for side loads, otherwise. Two subsets of data include full time histories of the loads. Runs 2963-2987 captured pure descent conditions for the CoPTR blades, during which the loads appeared highly transient, suggesting the possible presence of vortex ring state. Runs 3975-3998 captured data where the PTS actively yawed (pitched, from the proprotor's perspective) through the data point. These data files therefore include additional variables such as the tachometer signal and the PTS yaw time history. The PTS reported its position at a low sample rate, so the yaw variable was linearly interpolated and presented as steps in yaw; however, the actual yawing motion was smooth. The force and moment variables for these cases are organized the same as all other runs; however, each column represents a coefficient or load. A notes variable is included in each data file, which includes descriptions of the structures of the variables, the two runs used as pre- and post-run tares, and the date it was reduced.

6.2 Blade Geometries

Blade geometries will be released in two stages. The first stage contains as-drawn geometries and is available upon publication of this report. The second stage will include detailed laser scans of a subset of the blades as-tested and will be available at a later date as an addendum to this report. Hub geometries will also be released; however, proprietary hub designs will be genericized to protect the intellectual property of the manufacturers.

The as-drawn geometries for each blade/hub configuration are available as *.STEP* files. The blades and hubs in the files are combined as a single solid body for each file. This was done to protect proprietary hub designs where NASA may not own the internal geometries of the hubs and blade roots. Blade configurations that were tested with a spinner on the hub (COPR-G and CoPTR) also have the spinner as part of the released file. An example of the as-designed geometry is shown in Figure 48. Note that the tested spinners were fabricated as shells and not solid.

All blade sets tested in this entry were statically tested for failure due to centrifugal loading. The COPR-L, Ka1Gen, and 24", 28", and 36" COPR-G blades were all subjected to static pull testing by the manufacturers. These reports may be available upon request, pending approval from the manufacturers. The remaining blade sets (i.e. CoPTR, and 12" COPR-G) were tested internally and that information will be made available upon request. Each blade set was also tested by spinning to at least 120% of the maximum intended RPM.

Some relevant dimensions of the PTS are provided in this section to allow for the inclusion of the PTS vertical and horizontal sting components in modeling. The vertical sting of the PTS is a 9-inch diameter cylinder that is roughly 30 inches tall. The streamwise distance between the back face of the proprotor hubs and the leading edge of the vertical cylinder is 34 inches. The horizontal sting of the PTS begins at the end of the vertical sting. Moving upstream, it is a 7.325 inch cylinder at the junction, which tapers to a 6-inch diameter cylinder 22 inches downstream

from the back face of the proprotor hub. The final approximately 4.5 inches of the horizontal sting tapers down to the diameter of the PTS flange adapter, ≈3.4 inches. These dimensions are also provided in the schematic in Figure 9. The complete PTS assembly is intended to be included in the follow-on addendum with the as-built blade scans. A preliminary model of the complete PTS assembly is shown in Figure 49.

7 Concluding Remarks

An experimental test campaign was carried out in the NASA Langley Research Center's 14- by 22-Foot Subsonic Tunnel focused on measuring the performance and acoustic characteristics of proprotors for vertical lift applications. Ten proprotor configurations were tested at a variety of collective pitch angles in hover, cruise, and transitional flight conditions, totaling over 4,000 data points. These configurations included analytically-based designs typical of research work and designs that are more representative of the geometries found on UAM vehicles operating at full-scale. Major focuses of the test were an expansive operating envelope of cruise, arrival, and departure conditions as well as a scaling study which utilized multiple diameters of the same geometry. High quality acoustic measurements were collected via two microphones array, one focused on simultaneously capturing a range of directivities and a phased microphone array for source identification. This report documents the test campaign and describes the resulting experimental data that are now available to the broader research community.

References

1. Zawodny, N. S.; Pascioni, K. A.; and Thurman, C. S.: An Overview of the Proprotor Performance Test in the 14- by 22-Foot Subsonic Tunnel. *VFS International 79th Annual Forum & Technology Display*, West Palm Beach, FL, May 2023.

2. Zawodny, N. S.; Pettingill, N. A.; Lopes, L. V.; and Ingraham, D. J.: Experimental Validation of an Acoustically and Aerodynamically Optimized UAM Proprotor. Part 1: Test Setup and Results. NASA-TM-20220015637, National Aeronautics and Space Administration, 2023.

3. Zawodny, N. S.; Pascioni, K. A.; and Thurman, C. S.: An Overview of the Proprotor Performance Test in the 14- by 22-Foot Subsonic Tunnel. *Proceedings of the 79th Annual Forum of the Vertical Flight Society*, West Palm Beach, FL, 2023.

4. Manuel, G. S.; Molloy, J. K.; and Barna, P. S.: Effect of Collector Configuration on Test Section Turbulence Levels in an Open-Jet Wind Tunnel. NASA-TM-4333, National Aeronautics and Space Administration, 1992.

5. Zawodny, N. S.; Pascioni, K. A.; Lind, A. H.; Galles, M. B.; Stutz, C. M.; and Houston, M. L.: Reflectivity Characterization of In-Flow Acoustic Floor Treatment for the NASA Langley 14- by 22-Foot Subsonic Tunnel. *Inter-Noise 2024*, Nantes, France, August 2024.

6. Telecommunications and Timing Group: IRIG Serial Time Code Formats. IRIG STANDARD 200-04, Range Commanders Council, 2004.

7. Brucchieri, A.; Zawodny, N. S.; Houston, M. L.; and Stutz, C. M.: Comparative assessment of windscreen geometries for aeroacoustic measurements. *Noise-Con 2026*, Long Beach, CA, June 2026.

8. Stutz, C. M.; Houston, M. L.; Zawodny, N. S.; and Pascioni, K. A.: Acoustic Characterization of the NASA Langley 14- by 22-Foot Subsonic Tunnel Using Single-Microphone Analysis Techniques. *Noise-Con 2024*, New Orleans, LA, June 2024.

9. Martin, R. M.; Brooks, T. F.; and Hoad, D. R.: Reduction of Background Noise Induced by Wind Tunnel Jet Exit Vanes. *AIAA Journal*, vol. 23, no. 10, 1985, pp. 1631–1632.

10. Hu, X.; Luo, Y.; Leng, J.; Guo, P.; Yu, T.; and Wang, J.: The low frequency pressure pulsation and control of the open-jet wind tunnel. *Scientific Reports*, vol. 12, 2022, p. 19090.

11. Nance, D.; and Ahuja, K.: Limitations of the Three-Microphone Signal Enhancement Technique. *45th AIAA Aerospace Sciences Meeting and Exhibit*, Reno, NV, January 2007.

12. Reger, R.; Zawodny, N. S.; Pascioni, K.; Wetzel, D.; Liu, F.; and Cattafesta, L. N.: Design-Optimization of a Broadband Phased Microphone Array for Aeroacoustic Application. *Acoustical Society of America Meeting*, Hong Kong, China, May 2012.

13. Houston, M. L.; Stutz, C. M.; Zawodny, N. S.; and Pascioni, K. A.: Acoustic Characterization of the NASA Langley 14- by 22-Foot Subsonic Tunnel Using a Phased Array. *Noise-Con 2024*, New Orleans, LA, June 2024.

14. Figliola, R. S.; and Beasley, D. E.: *Theory and Design for Mechanical Measurements*, John Wiley and Sons, New York, 5. 5 ed., 2012.

15. Tinney, C. E.; and Valdez, J. A.: Hover Performance and Acoustics of a 35Scale Notional eVTOL Rotor. *30th AIAA/CEAS Aeroacoustics Conference*, Rome, Italy, June 2024.

16. Tinney, C. E.; and Valdez, J. A.: Optimum Hover Conditions for Reduced Noise From a Notional eVTOL Rotor. *AIAA Aviation Forum*, Las Vega, NV, July 2025.

17. Houston, M. L.; Pascioni, K. A.; Stutz, C. M.; and Stephenson, J. H.: Snapshot Array Design Considerations for Rotorcraft Noise Characterization. *Proceedings of the 81st Annual Forum of the Vertical Flight Society*, May 2025.

18. Heath, S.; Brooks, T.; Hutchenson, F. V.; Doty, M. J.; Haskin, H.; Spalt, T.; Bahr, C. J.; Burley, C. L.; Bartram, S.; Humphreys, W.; Lunsford, C.; Pepernack, T.; Colbert, S.; Hoad, D.; Becker, L.; Stead, D.; Kutcha, D.; and Yeh, L.: Hybrid Wing Body Aircraft Acoustic Test Preparations and Facility Upgrades. *AIAA Ground Testing Conference*, San Diego, CA, June 2013.

19. Brooks, T. F.; and Humphreys, W. M.: A Deconvolution Approach for the Mapping of Acoustic Sources (DAMAS) determined from Phased Microphone Arrays. *Journal of Sound and Vibration*, vol. 294, 2006, pp. 865 – 879.

20. Sijtsma, P.: Location of Rotating Sources by Phased Array Measurements. *7th AIAA/CEAS Aeroacoustics Conference and Exhibit*, Maastricht, Netherlands, May 2001.

21. Acoustical Vibrations Engineering Consultants Inc.: *Phased Array Software Version 5.15 User Manual*. 2022. Www.avec-engineering.com.

Tables

Table 1: Summary of test articles.

Geometry Name	Geometry Acronym	Diameter (in)	N_b
Computationally-Optimized Proprotor, LaRC Tip	COPR-L	24	3, 5
Computationally-Optimized Proprotor, GRC Tip	COPR-G	12, 24, 28, 36	2, 4
Commercial Prototype TiltRotor	CoPTR	24	5
Kinetic Analytics 1st Generation	KA1Gen	24	3

Table 2: Radial locations of collective angle settings.

Blades	COPR-L	COPR-G	CoPTR	KA1Gen
r/R	0.56	0.75	0.75	0.75
β'_{offset} (°)	-7.4	0	0	0

Table 3: Collected data sets for COPR-L configurations, $D = 24$".

N_b	Run Type	β' (°)	α_p (°)	Trip Height (mil)
5	Hover	14.6, 17.6, 19.8	0	0
	Cruise	35.1	0	0
	Edgewise	25.1	30-50	0
3	Hover	10.6, 12.1, 13.6, 17.6, 20.6	0	0
	Hover	13.1, 13.6, 17.6	0	3.1, 6.0, 9.9
	Cruise	35.1	0	0

Table 4: Collected data sets for COPR-G configurations.

N_b	Diameter (in)	Run Type	β' (°)	α_p (°)
4	12, 24, 28	Hover	11.5	0, 45
	12, 24, 28	Cruise	35.3	0
	12, 24, 28	Edgewise	11.5	45
2	36	Hover	5.5	0
	12, 24, 36	Hover	7.5, 9.5, 11.5, 13.5, 15.5, 17.5	0
	12, 24, 36	Hover	11.5	45
	12, 24, 36	Cruise	32.8	0
	12, 24, 36	Edgewise	11.5	45

Table 5: Collected data sets for CoPTR blades, $D = 24$", $N_b = 5$.

Run Type	β' (°)	α_p (°)
Hover	-16, 12, 16, 20	0
Cruise	30	0
Climb	16	0
Descent	-16	0
Departure	30	5-20
	25	20-45
	20	30-60
	16	45-88
Approach	25	10-80
	10	80-88
	5	65-80
	-16	92-100*

*Actual tested pitch angles were 180° - α_p

Table 6: Collected data sets for KA1Gen blades, $D = 24$", $N_b = 3$.

Run Type	β' (°)	α_p (°)	Trip Height (mil)
Hover	8.3, 9, 12, 15	0	0
Hover	9	0	3.1
Cruise	25, 30.5	0	0
Cruise	25	0	3.1
Edgewise	6	70, 80	0

Table 7: Phased array coordinates, where $+x$ is streamwise, $+y$ is up, and $+z$ is into the array face.

Mic.	x (in)	y (in)	z (in)	Mic.	x (in)	y (in)	z (in)
1	9.0700	22.4200	-0.5200	29	8.8400	12.9900	-0.3700
2	21.3200	11.8200	-0.7400	30	14.7400	4.0300	-0.4100
3	23.8600	-4.8500	-0.7700	31	13.8200	-6.1600	-0.4500
4	15.1000	-18.9000	-0.3400	32	6.3400	-13.5900	-0.2400
5	-0.5600	-23.9200	0.1100	33	-3.7000	-14.4900	0.0700
6	-15.8900	-17.9000	0.5800	34	-12.3800	-8.5600	0.3500
7	-23.8600	-3.5600	0.6300	35	-14.9900	1.3600	0.4300
8	-20.4800	12.5100	0.4300	36	-10.7700	10.7200	0.1700
9	-7.6000	22.9300	-0.0300	37	-4.1500	10.4600	-0.0500
10	1.4400	18.0000	-0.2600	38	3.3100	10.8700	-0.2700
11	12.9900	12.9400	-0.4800	39	9.3400	5.9900	-0.3600
12	18.1500	1.7500	-0.4900	40	11.2000	-1.4700	-0.4400
13	14.7400	-10.4100	-0.3900	41	7.6800	-8.1600	-0.2700
14	4.5800	-17.3100	-0.1400	42	0.5000	-11.0600	-0.1500
15	-7.6500	-16.2000	0.2400	43	-6.8500	-8.8100	0.1600
16	-16.4200	-7.5300	0.4900	44	-11.0600	-2.2700	0.2700
17	-17.4200	4.8500	0.4300	45	-9.8800	5.2500	0.0600
18	-10.4800	14.6100	0.1900	46	-3.4200	0.0800	-0.1100
19	0.4000	16.8200	-0.0600	47	-2.7200	2.1900	-0.1700
20	11.3600	12.8800	-0.4900	48	-0.6000	3.4200	-0.2600
21	16.7700	2.6000	-0.5400	49	1.6300	3.2200	-0.1500
22	14.6000	-8.9200	-0.4000	50	3.2900	1.2900	-0.1900
23	5.2700	-16.1100	-0.1600	51	2.8700	-0.8200	-0.1900
24	-6.2800	-15.8800	0.2200	52	1.7100	-2.7100	-0.0900
25	-15.0900	-8.1000	0.5000	53	-0.6900	-3.1100	-0.1800
26	-16.7700	3.5500	0.4100	54	-2.4500	-2.2900	-0.1800
27	-10.5600	13.4100	0.2000	**55**	**0.0000**	**0.0000**	**0.0000**
28	-1.6500	15.3500	-0.0500	PTS Flange	42.520	14.567	-180.709

Table 8: Speaker waveforms.

Waveform Name	Type	Frequency Range	Period
B1	Band-limited white noise	100 Hz - 10 kHz	60 s
B2	Band-limited white noise	300 Hz - 10 kHz	60 s
B3	Band-limited white noise	5 kHz - 20 kHz	60 s
B4	Band-limited white noise	38 Hz - 24,373 Hz	60 s
B5	Band-limited white noise	224 Hz - 17,780 Hz	60 s
I1	Impulse	2,536 Hz center	0.5 s
I2	Impulse	5,076 Hz center	0.5 s
M1	"Multisine"	100 Hz - 10 kHz	0.5 s
M2	"Multisine"	300 Hz - 10 kHz	0.5 s
M4	"Multisine"	5 kHz - 20 kHz	0.5 s
M5	"Multisine"	100 Hz - 20 kHz	0.5 s
C1	Modulated tone	3 kHz center	0.25 s

Table 9: Propeller vs. Rotor Dimensionless Parameters.

Variable Name	Propeller	Rotor	Conversion
Thrust	$C_{T,p} = \frac{4\pi^2 T}{\rho\Omega^2 D^4}$	$C_{T,r} = \frac{16T}{\pi\rho\Omega^2 D^4}$	$C_{T,r} = \frac{4}{\pi^3} C_{T,p}$
Power	$C_{P,p} = \frac{8\pi^3 Q}{\rho\Omega^2 D^5}$	$C_{P,r} = \frac{32Q}{\pi\rho\Omega^2 D^5}$	$C_{P,r} = \frac{4}{\pi^4} C_{P,p}$
Normal Force	$C_{N,p} = \frac{4\pi^2 N}{\rho\Omega^2 D^4}$	$C_{N,r} = \frac{16N}{\pi\rho\Omega^2 D^4}$	$C_{N,r} = \frac{4}{\pi^3} C_{N,p}$
Side Force	$C_{Y,p} = \frac{4\pi^2 Y}{\rho\Omega^2 D^4}$	$C_{Y,r} = \frac{16Y}{\pi\rho\Omega^2 D^4}$	$C_{Y,r} = \frac{4}{\pi^3} C_{Y,p}$
Pitching Moment	$C_{m,p} = \frac{4\pi^2 m}{\rho\Omega^2 D^5}$	$C_{m,r} = \frac{32m}{\pi\rho\Omega^2 D^5}$	$C_{m,r} = \frac{8}{\pi^3} C_{m,p}$
Yawing Moment	$C_{n,p} = \frac{4\pi^2 n}{\rho\Omega^2 D^5}$	$C_{n,r} = \frac{32n}{\pi\rho\Omega^2 D^5}$	$C_{n,r} = \frac{8}{\pi^3} C_{n,p}$
Advance Ratio	$J = \frac{\pi U_\infty}{\Omega R}$	$\mu = \frac{U_\infty}{\Omega R} cos\alpha_{TPP} = \frac{U_\infty}{\Omega R} sin\alpha_P$	$\mu = \frac{1}{\pi} J sin\alpha_P$
Eff. Advance Ratio	$J_{\text{eff}} = J cos\alpha_P$		$\mu = \frac{1}{\pi} J_{\text{eff}} tan\alpha_P$
Propellor Efficiency	$\eta = \frac{C_{T,p}}{C_{P,p}} J$		
Prop. Axial Efficiency	$\eta_x = \frac{C_{T,p} cos\alpha_P - C_{N,p} sin\alpha_P}{C_{P,p}} J$		
Rotor Lift to Drag		$\frac{L}{D} = \frac{TU_\infty cos\alpha_{TPP}}{\Omega Q} = \frac{TU_\infty sin\alpha_P}{\Omega Q}$	$\frac{L}{D} = \frac{C_{T,p}}{C_{P,p}} J sin\alpha_P = \frac{C_{T,r}}{C_{P,r}} \mu$
Figure of Merit	$FM = \frac{2C_{T,p}^{3/2}}{\sqrt{2\pi} C_{P,p}}$	$FM = \frac{C_{T,r}^{3/2}}{\sqrt{2} C_{P,r}}$	

Table 10: Guide for Applying Microphone Corrections.

Microphone Set	Mic Numbers	Corrections	Notes
Grid Array	Grid Array 1-30	Incidence Angle, Atmospheric Attenuation	Grid caps all removed
Three-Mic Clusters	Grid Array 31-36	Grid Cap, Atmospheric Attenuation	Mounted pointing at source
Phased Array	Phased Array 1-54	Incidence Angle, Atmospheric Attenuation	Optional, constant across array, fused grid caps
Phased Array Reference Mic	Grid Array 37 & Phased Array 55	Incidence Angle, Atmospheric Attenuation	Grid cap removed

Table 11: Data subset to be hosted online.

Blades	Regime	β' (°)	M_{tip}	M_∞	α_p (°)	J_{eff}	Run No.
CoPTR	Hover	12	0.350	0	0	0	633
		16	0.350	0	0	0	581
		20	0.350	0	0	0	615
	Depart.	16	0.365	0.015	88	0.005	1005
		16	0.364	0.030	80	0.045	977
		20	0.370	0.060	70	0.174	936
	Cruise	30	0.413	0.145	0	1.103	3963
		30	0.380	0.085	0	0.703	3967
	Approach	5	0.414	0.085	70	0.221	2561
		10	0.415	0.060	80	0.079	2612
		16	0.36	0.040	88	0.012	1011
		16	0.364	0.030	92	-0.009	2863
		16	0.364	0.030	96	-0.027	2905
		16	0.374	0.015	100	-0.022	2942
KA1Gen	Hover	8.3	0.400	0	0	0	3267
		9	0.400	0	0	0	3154
		12	0.400	0	0	0	3178
		15	0.400	0	0	0	3204
	Cruise	25	0.377	0.060	0	0.500	3891
		25 (tripped)	0.377	0.060	0	0.500	3836
		30.5	0.377	0.060	0	0.500	3320
	Transition	6	0.479	0.100	70	0.224	3452
		6	0.500	0.040	80	0.044	3422

Table 12: Description of Microphone Data Files.

Variable Name	Description	Units
BPF	Blade passage frequency	
Diameter	Blade diameter	feet
Nb	Number of blades	
Params	Parameters structure	
Params.c0_humid	Humid speed of sound	m/s
Params.dew_tc	Test cell dewpoint	°C
Params.Fs	Sample rate	
Params.humid_tc	Test cell humidity	%
Params.Nch	Number of channels	
Params.Nsamp	Number of samples	
Params.P_tc	Test cell ambient pressure	Pascal
Params.rho_humid	Humid air density	kg/m^3
Params.Roll	PTS roll encoder	°
Params.T_tc	Test cell ambient temperature	°C
Params.vel	Freestream velocity	m/s
Params.Yaw	PTS yaw encoder	°
PressData	[Nsamp,Nch] array of microphone data	Pascal
tach	Tachometer signal	Volts
time	Created from Fs and Nsamp	seconds
Tsync	Time sync pulse	volts
Wvfm	Commanded speaker waveform	volts

Table 13: Description of Steady Load Data Files.

Variable Name	Description	Units
CoeffUncert	Load coefficient uncertainties, $[uC_{N,p}, uC_{Y,p}, uC_{T,p}, uC_{m,p}, uC_{n,p}, uC_{P,p}, uFM, u\eta]$	
loadCoeffs	Load coefficients, $[C_{N,p}, C_{Y,p}, C_{T,p}, C_{m,p}, C_{n,p}, C_{P,p}, FM, \eta_x]$	
loads	Dimensional loads, $[F_x, F_y, F_z, M_x, M_y, M_z, N, Y, n, m]$	inch, inch-lbf
Params	Parameters structure	
Params.b_rho	Air density bias uncertainty	kg/m^3
Params.b_Uinf	Freestream speed bias uncertainty	m/s
Params.c0_humid	Humid speed of sound	m/s
Params.dew_tc	Test cell dewpoint	°C
Params.Fs	Sample rate	
Params.humid_tc	Test cell humidity	%
Params.Nch	Number of channels	
Params.Nsamp	Number of samples	
Params.P_tc	Test cell ambient pressure	Pascal
Params.rho_humid	Humid air density	kg/m^3
Params.Roll	PTS roll encoder	°
Params.s_rho	Air density random uncertainty	kg/m^3
Params.s_Uinf	Freestream speed random uncertainty	m/s
Params.T_tc	Test cell ambient temperature	°C
Params.vel	Freestream velocity	m/s
Params.Yaw	PTS yaw encoder	°
speeds	Speed parameters $[M_\infty, M_{tip}, J, J_{\text{eff}}, \omega, RPM]$	ω in rad/s

Table 14: Description of Unsteady Load Data Files.

Variable Name	Description	Units
Jeff	Effective advance ratio	
loadCoeffs	[Nsamp, 8] Array of load coefficients, $[C_{N,p}, C_{Y,p}, C_{T,p}, C_{m,p}, C_{n,p}, C_{P,p}, FM, \eta_x]$	
loads	[Nsamp, 10] array of dimensional loads, $[F_x, F_y, F_z, M_x, M_y, M_z, N, Y, n, m]$	inch, inch-lbf
Params	Parameters structure	
Params.b_rho	Air density bias uncertainty	kg/m^3
Params.b_Uinf	Freestream speed bias uncertainty	m/s
Params.c0_humid	Humid speed of sound	m/s
Params.dew_tc	Test cell dewpoint	°C
Params.Fs	Sample rate	
Params.humid_tc	Test cell humidity	%
Params.Nch	Number of channels	
Params.Nsamp	Number of samples	
Params.P_tc	Test cell ambient pressure	Pascal
Params.rho_humid	Humid air density	kg/m^3
Params.Roll	PTS roll encoder	°
Params.s_rho	Air density random uncertainty	kg/m^3
Params.s_Uinf	Freestream speed random uncertainty	m/s
Params.T_tc	Test cell ambient temperature	°C
Params.vel	Freestream velocity	m/s
Params.Yaw	PTS yaw encoder	°
speeds	Mean speed parameters, $[M_\infty, M_{tip}, J, J_{\text{eff}}, \omega, RPM]$	ω in rad/s
tach	Tachometer signal	Volts
time	Created from Fs and Nsamp	seconds
Tsync	Time sync pulse	volts
Yaw_interp	Interpolated PTS yaw encoder	°

Figures

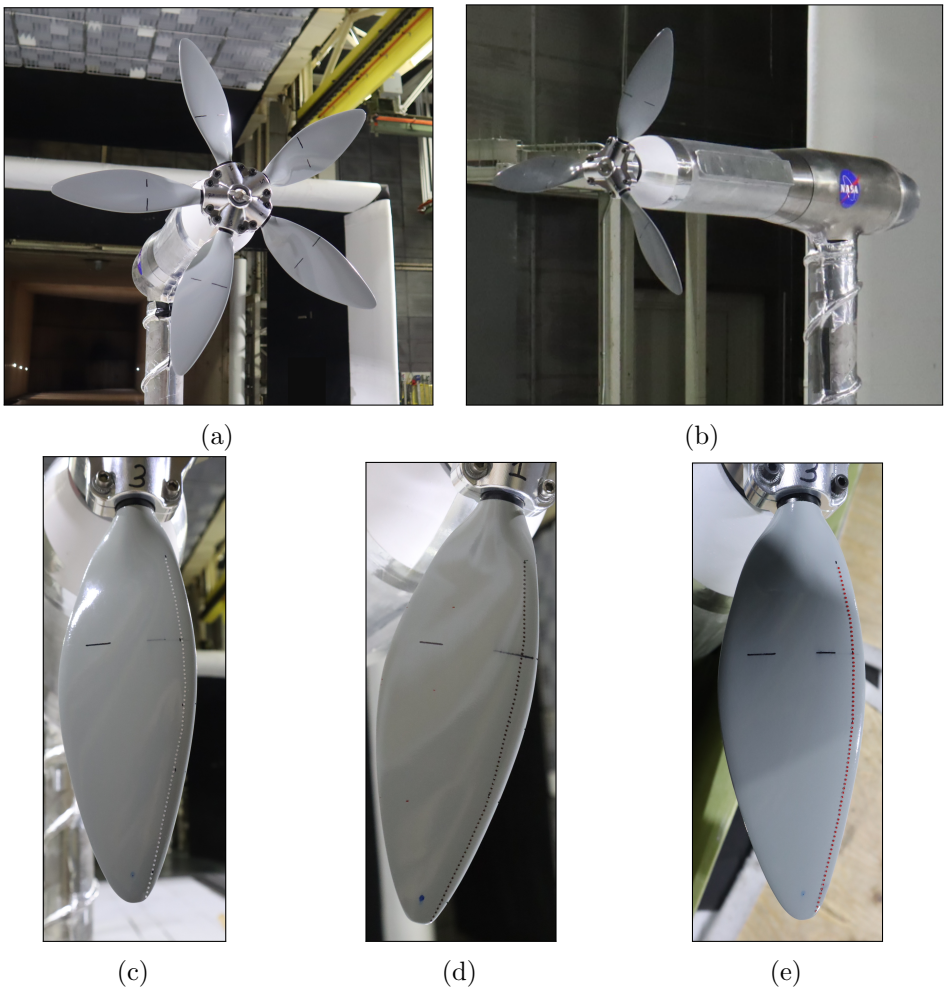
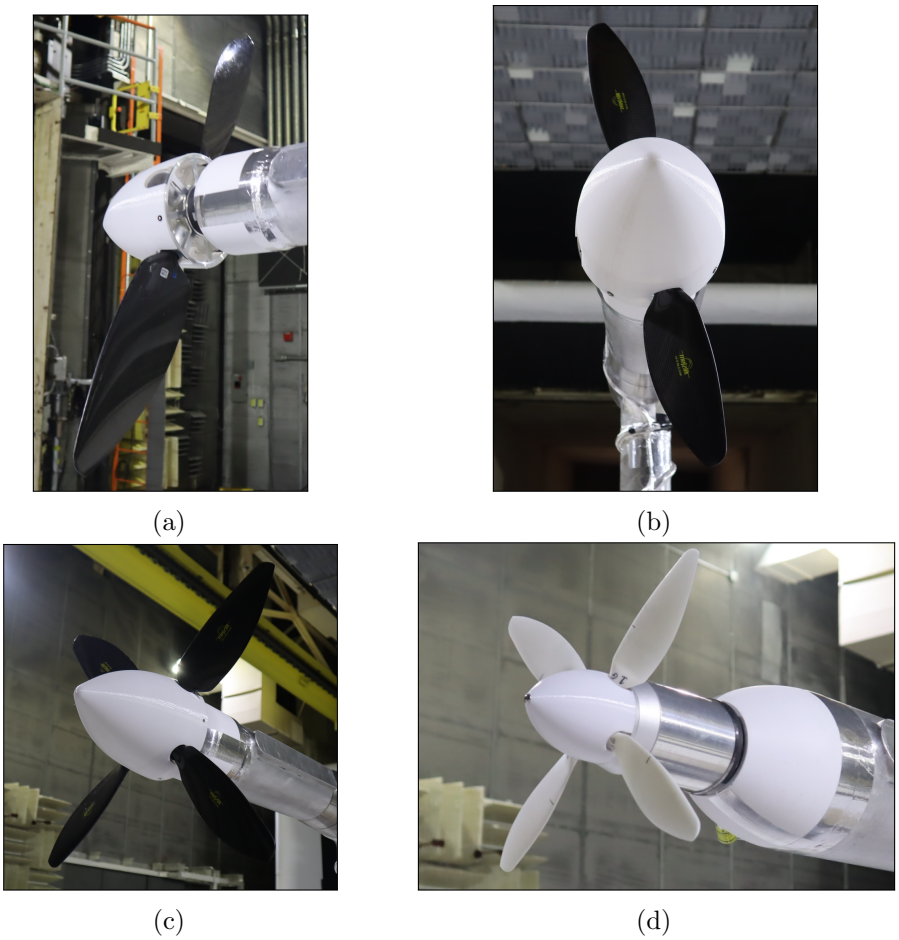


Figure 1: COPR-L blades in (a) clean COPR5-L configuration without a spinner and COPR3-L with (b) no trip dots, (c) 3.1 mil trip dots, (d) 6 mil trip dots, and (e) 9.9 mil trip dots without a spinner. (*Source: NASA*)



(a) (b) (c) (d)

Figure 2: COPR-G configurations: (a) 36" COPR2-G, (b) 24" COPR2-G, (c) 28" COPR4-G, and (d) 12" COPR4-G. (*Source: NASA*)

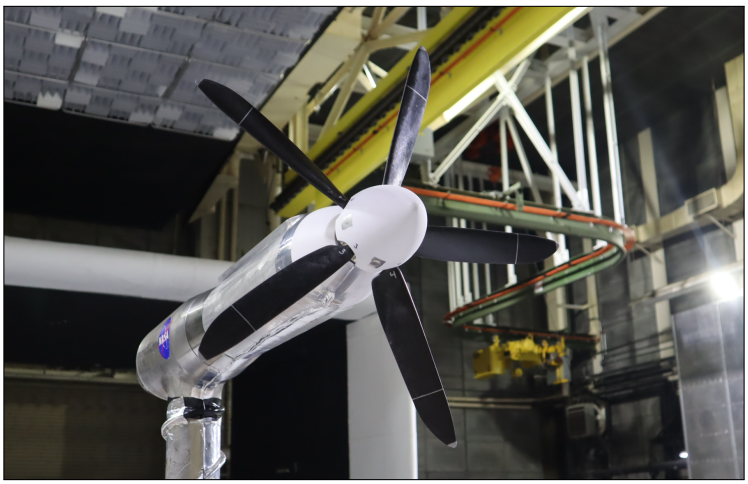
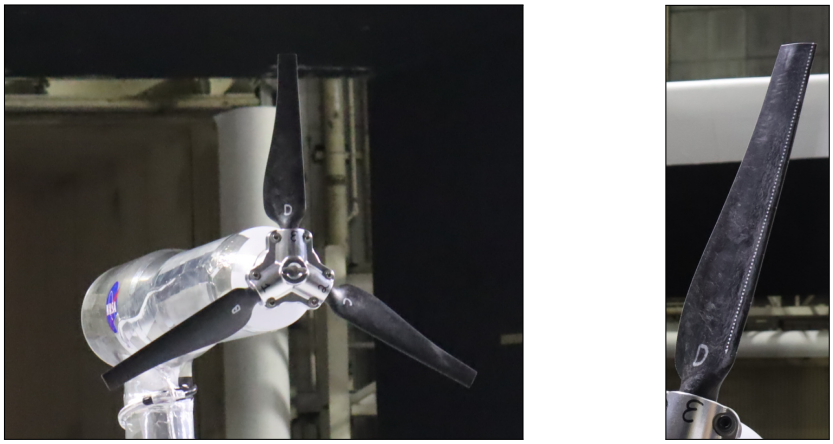


Figure 3: CoPTR blades. (*Source: NASA*)



(a) (b)

Figure 4: KA1Gen blades (a) without and (b) with 3.1 mil trip dots. (*Source: NASA*)



Figure 5: Example of collective angle adjustment using pitch block on CoPTR blades. (*Source: NASA*)

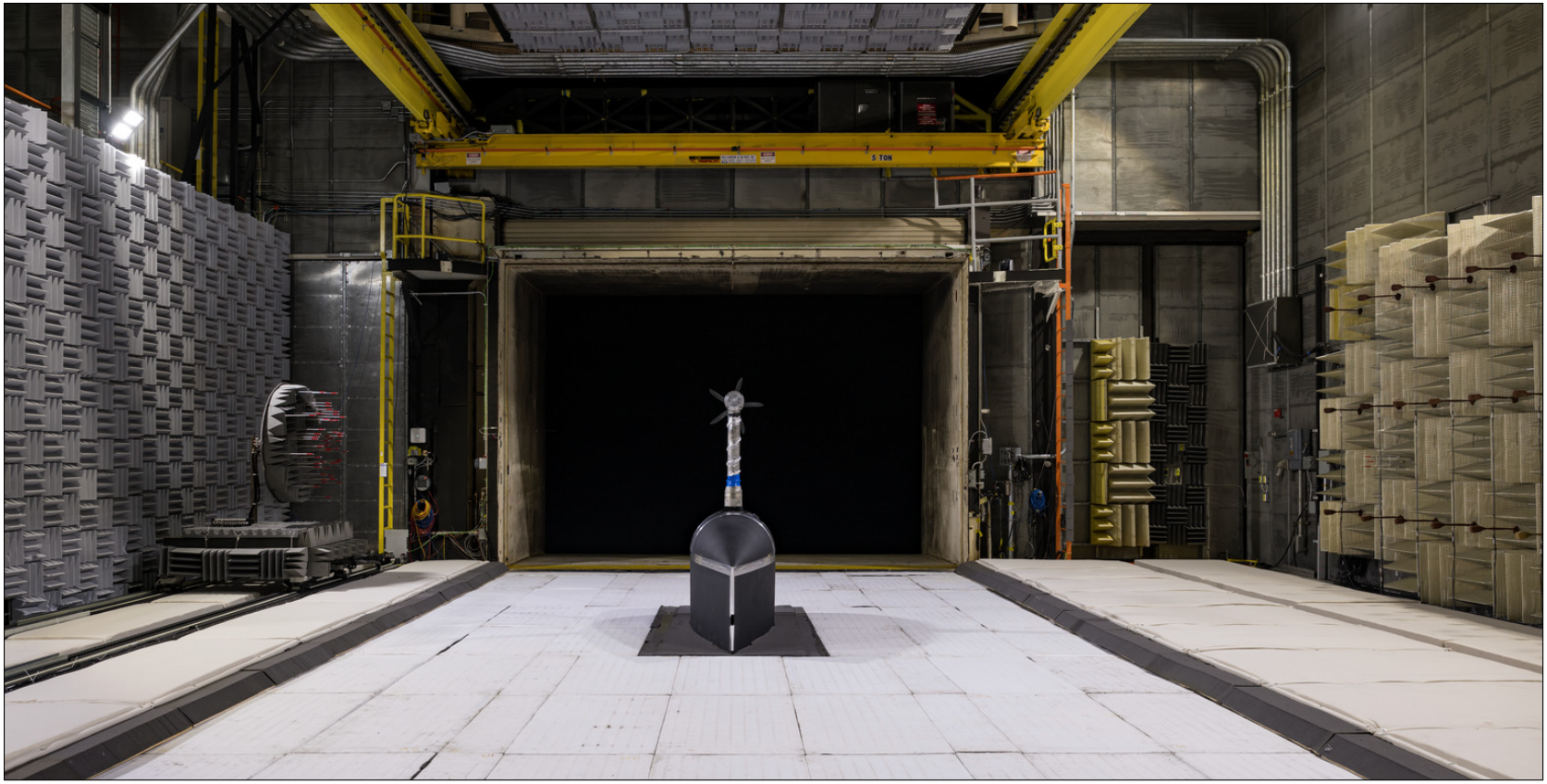
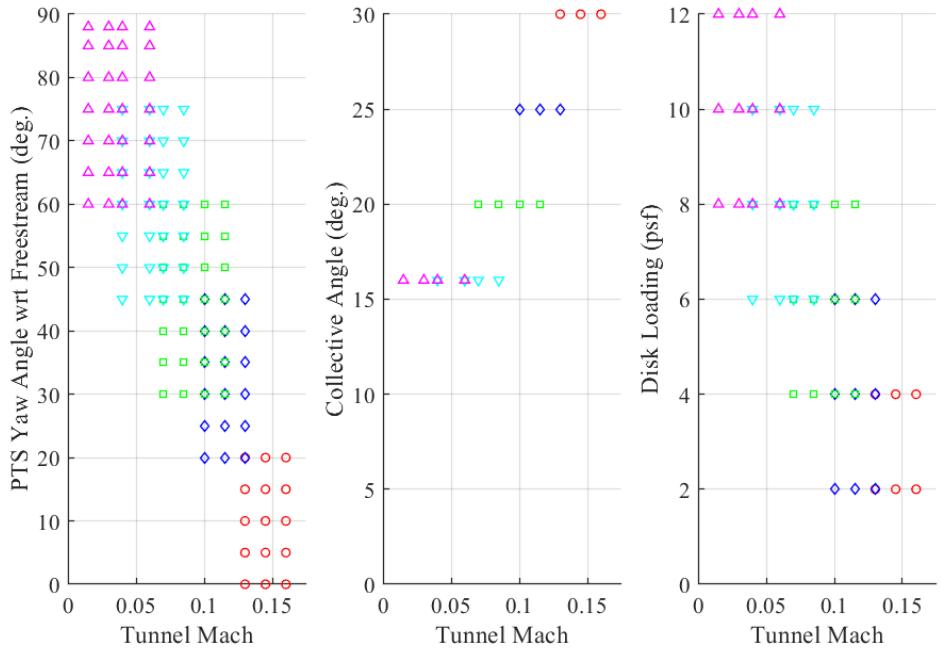
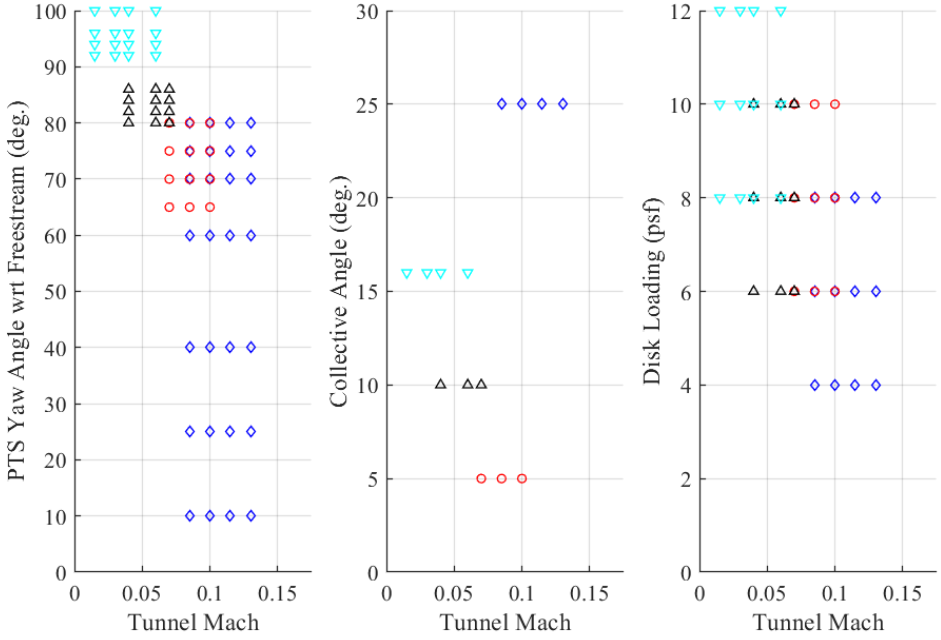


Figure 6: Test section of 14- by 22-Foot Subsonic Tunnel during VLPNT (looking upstream). (*Source: NASA*)

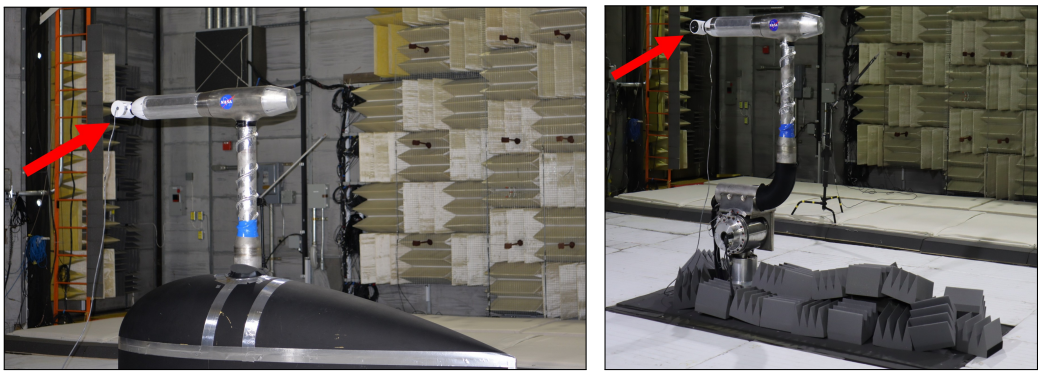


(a)



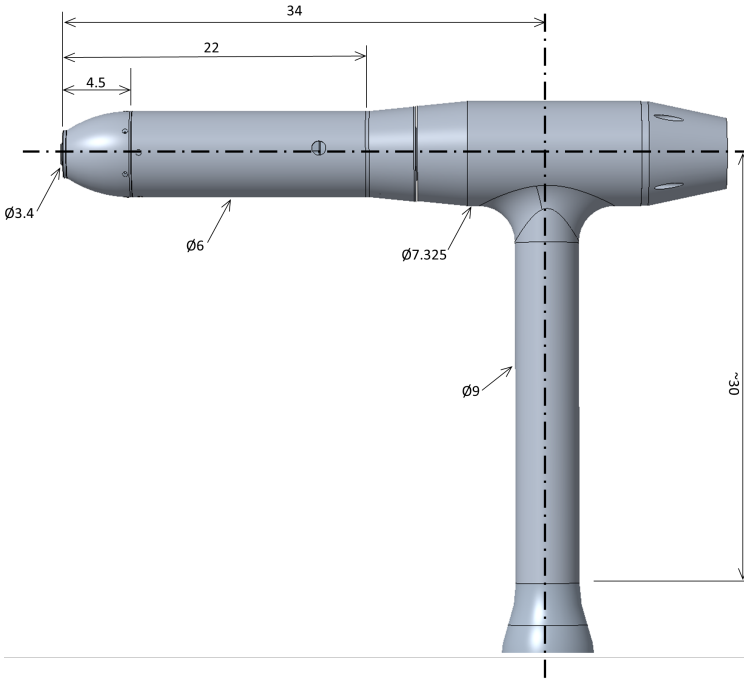
(b)

Figure 7: Planned points for (a) departure and (b) approach transition profiles for CoPTR blades. Note that symbol combinations are common across the three plots for each type of run conditions.

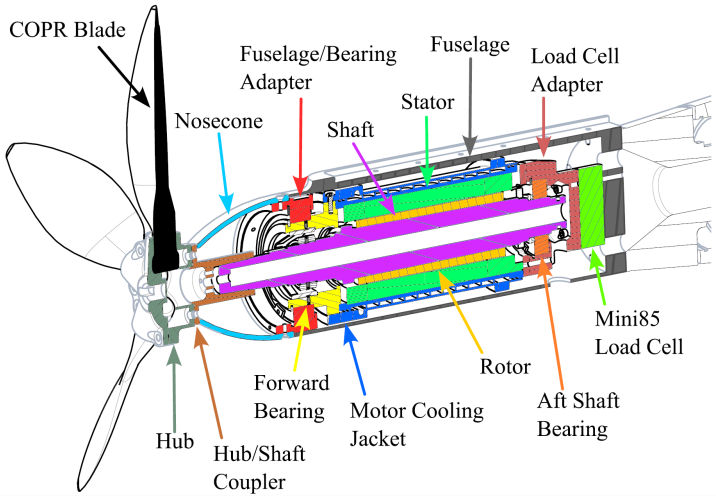


(a) (b)

Figure 8: Speaker (indicated by arrows) mounted to PTS flange for reflection assessment (a) with and (b) without the fairing. (*Source: NASA*)



(a)



(b)

Figure 9: Schematics of (a) PTS dimensions (in inches) and (b) PTS internals. (*Source: NASA*)

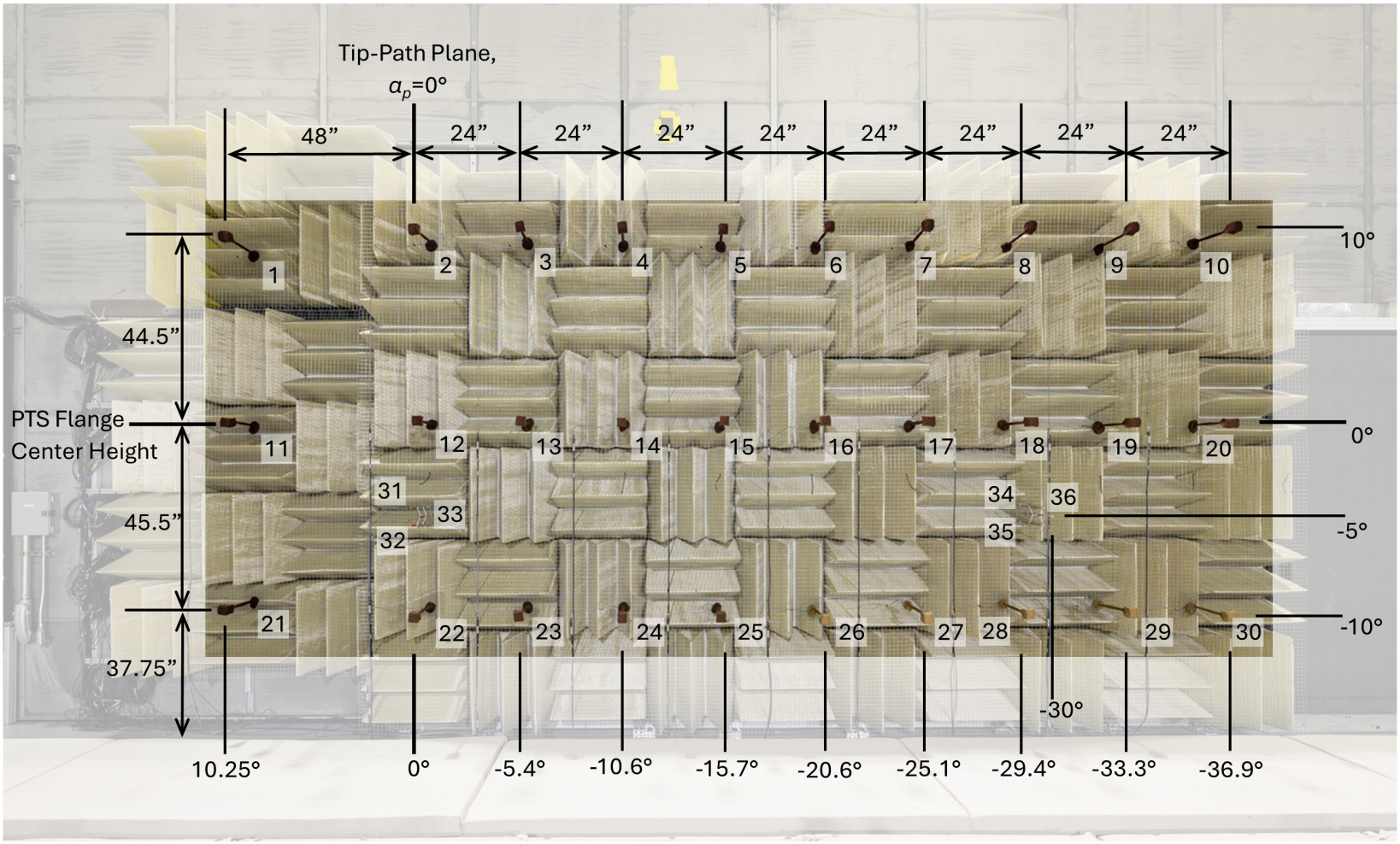
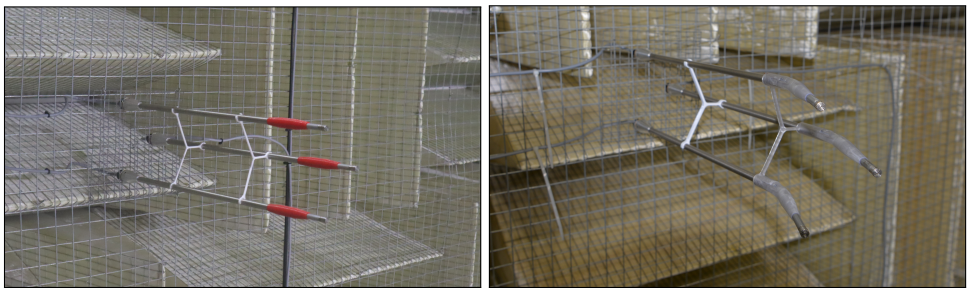


Figure 10: Grid array of microphones. (*Source: NASA*)



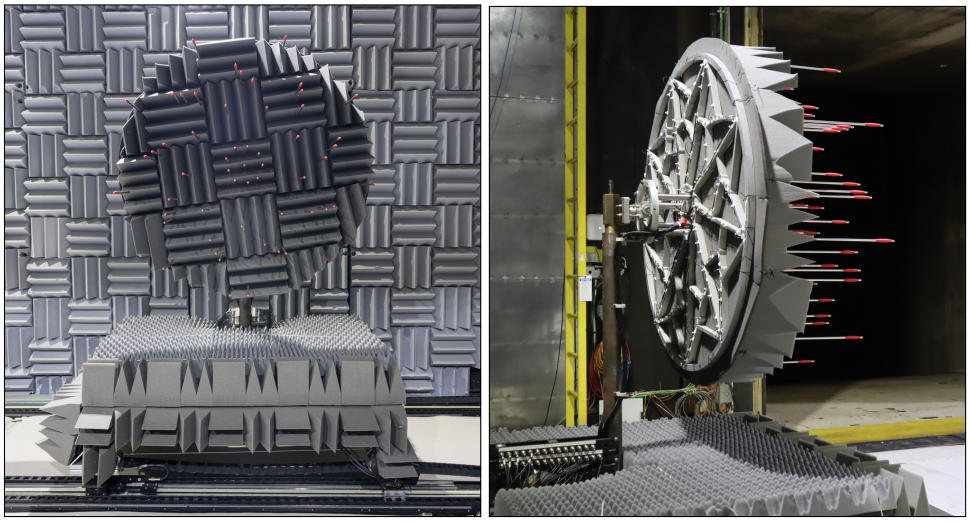
(a) (b)

Figure 11: Grid array microphone mounting (a) without and (b) with windscreens. Note grid caps were removed before installing windscreen. (*Source: NASA*)



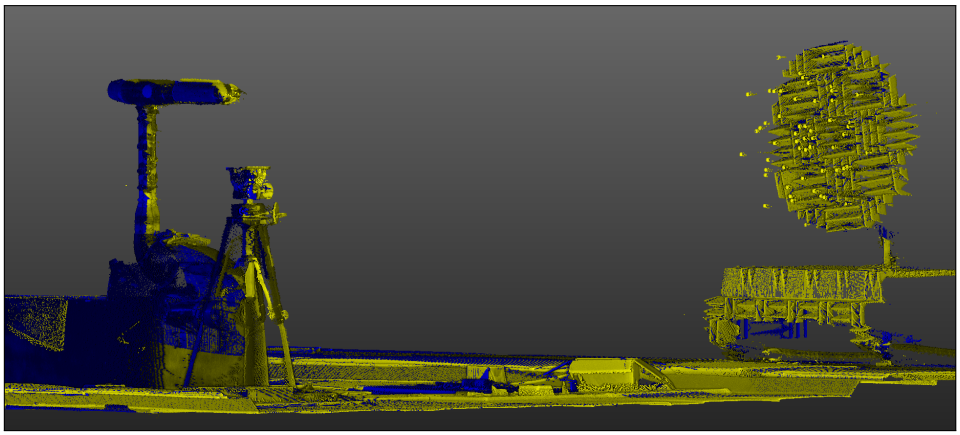
(a) (b)

Figure 12: Grid array microphone mounting for (a) upstream and (b) downstream three-microphone clusters. (*Source: NASA*)

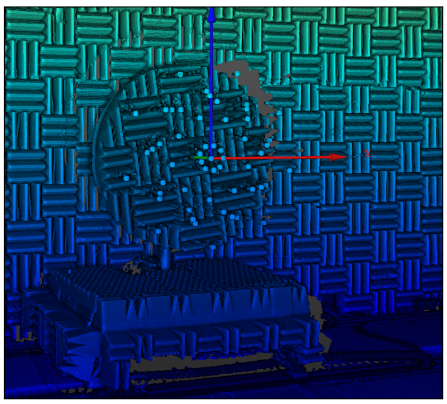


(a) (b)

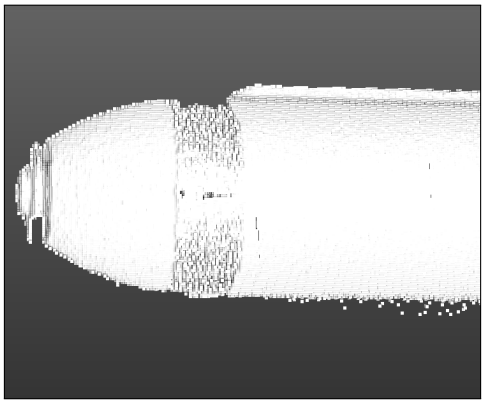
Figure 13: North wall phased array. (*Source: NASA*)



(a)



(b)



(c)

Figure 14: Sample images of the laser scan results showing (a) the PTS relative to the phased array, (b) the phased array, and (c) the PTS flange. (*Source: NASA*)

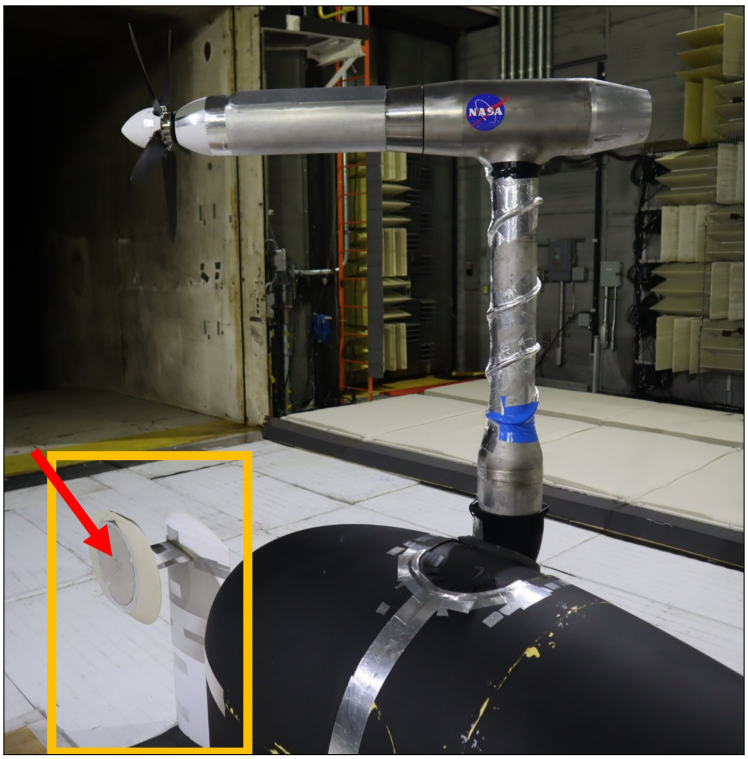


Figure 15: Inflow speaker source (red arrow) in aerodynamic fairing (yellow box). (*Source: NASA*)

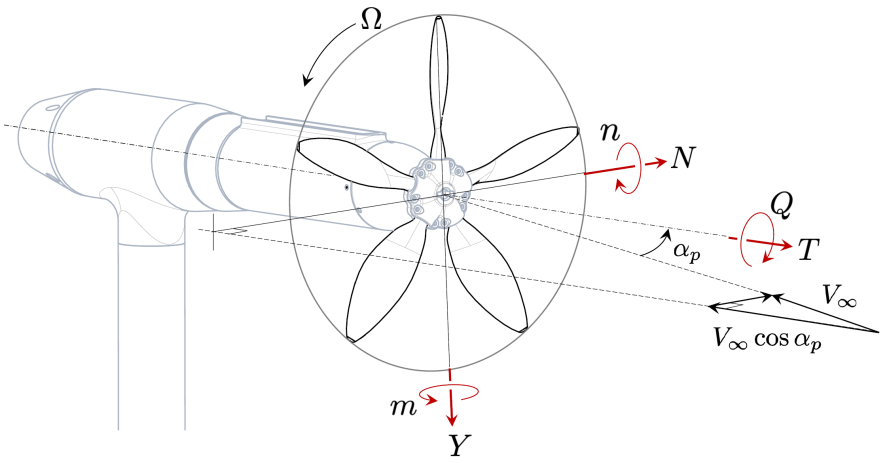


Figure 16: Propellor conventions for forces and moments. (*Source: NASA*)

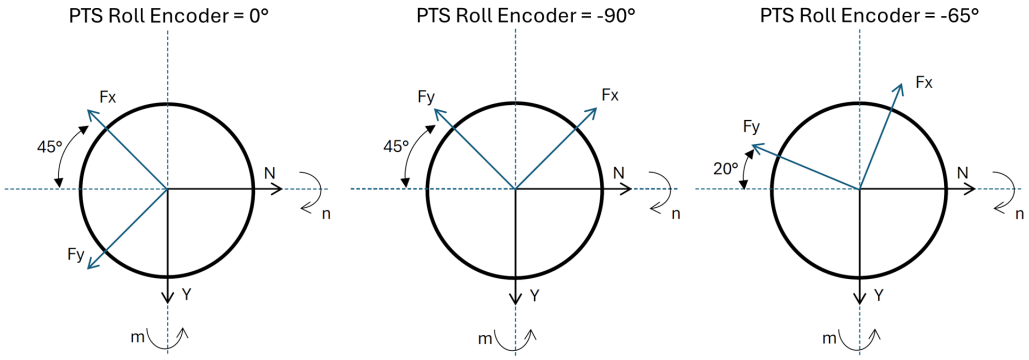


Figure 17: Load cell axis orientations based on PTS roll encoder setting, looking at PTS from test section inlet. (*Source: NASA*)

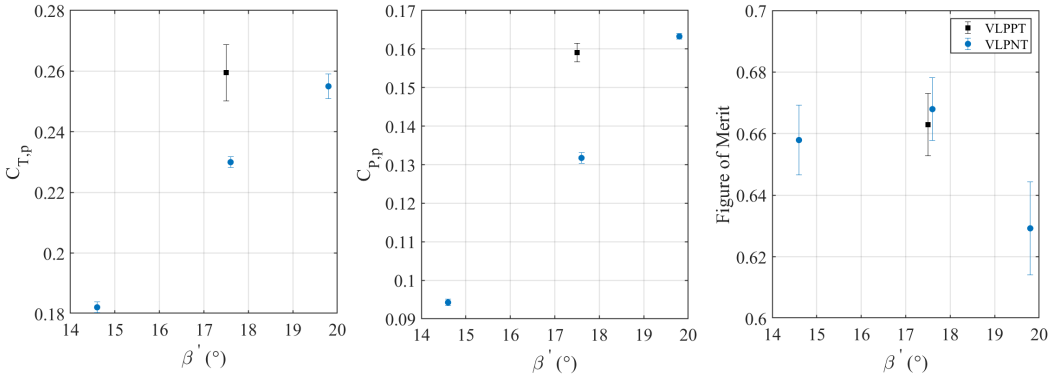


Figure 18: COPR5-L hover performance at M_{tip}=0.300 from VLPPT and VLPNT.

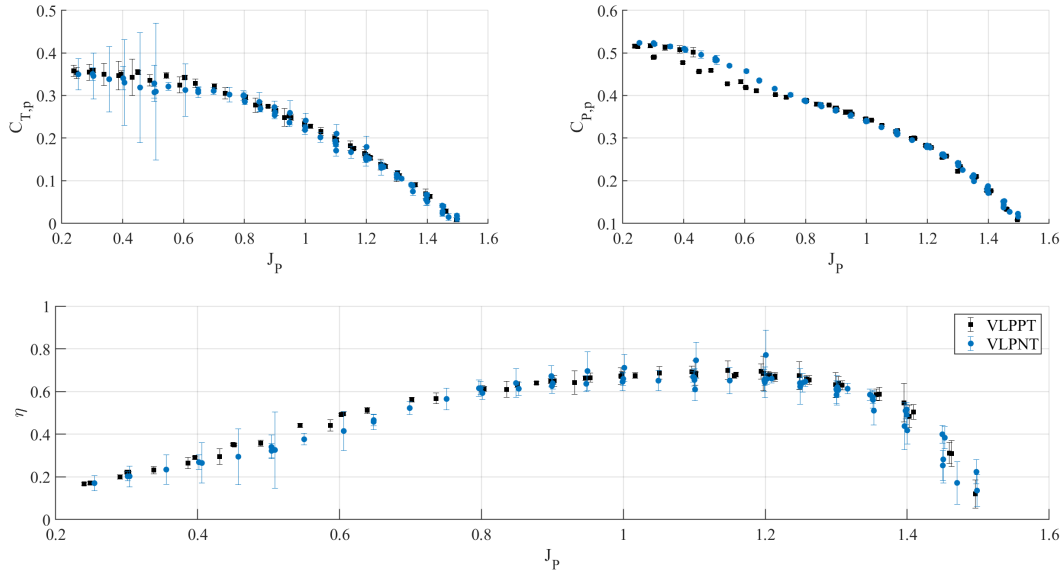


Figure 19: COPR5-L cruise performance from VLPPT and VLPNT.

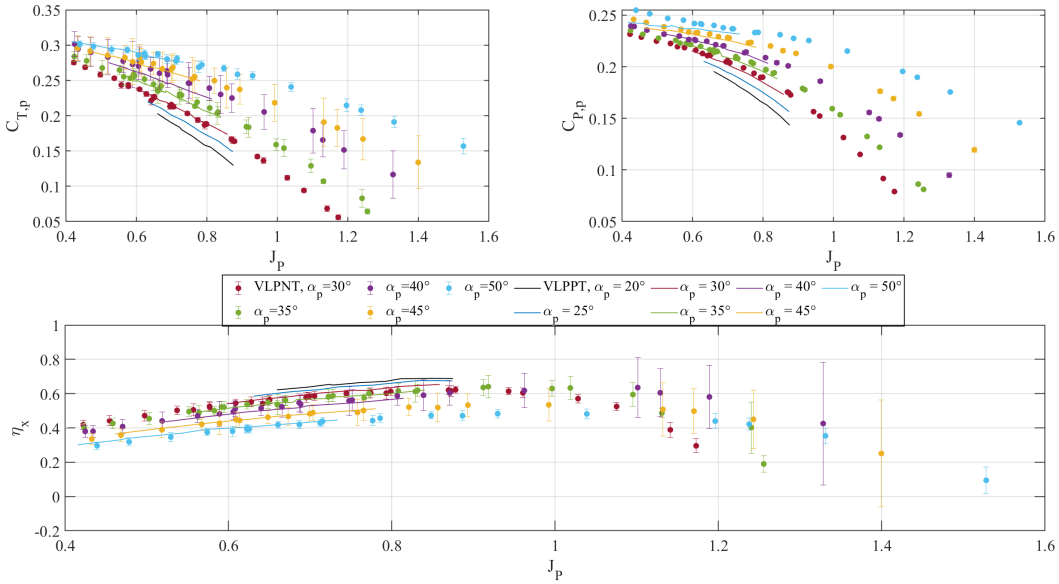


Figure 20: COPR5-L edgewise conditions from VLPPT and VLPNT.

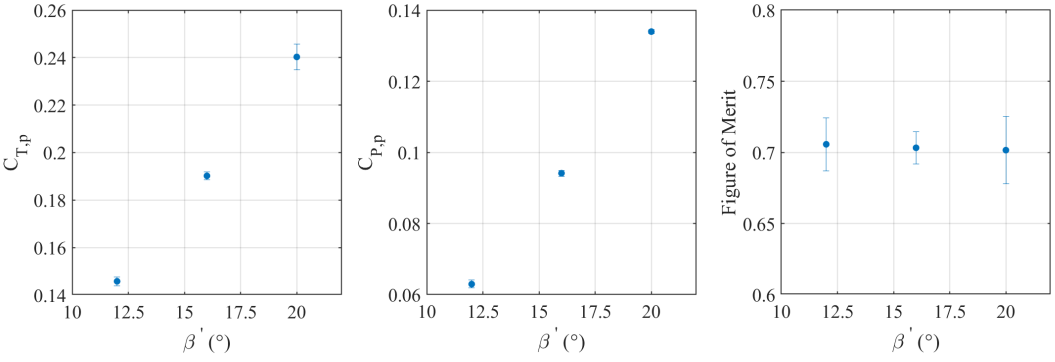


Figure 21: CoPTR hover performance at M_{tip}=0.300 .

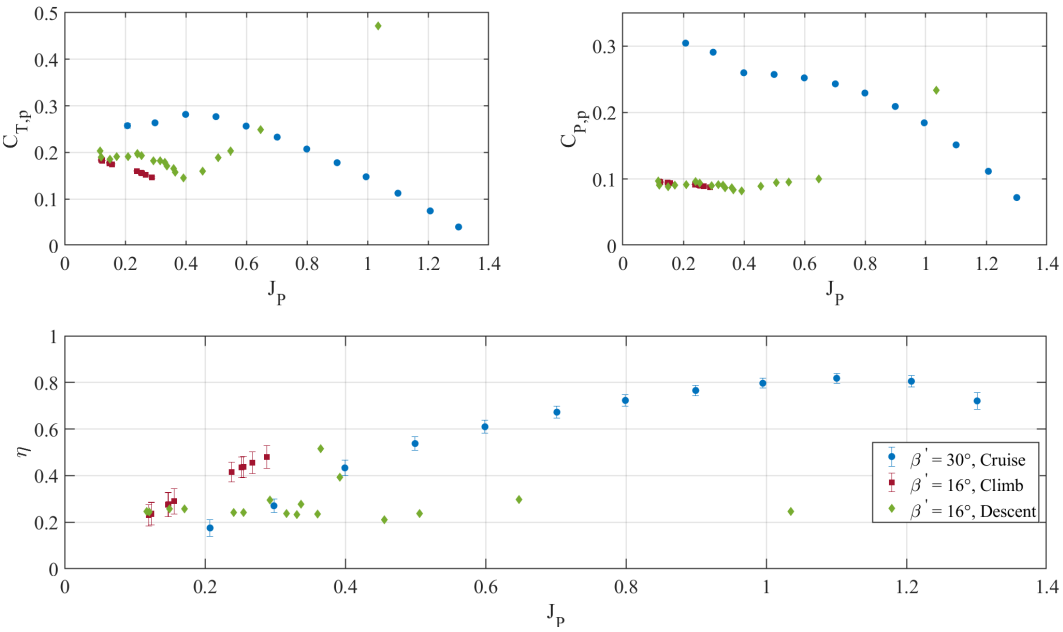


Figure 22: Axial flight performance of CoPTR blades.

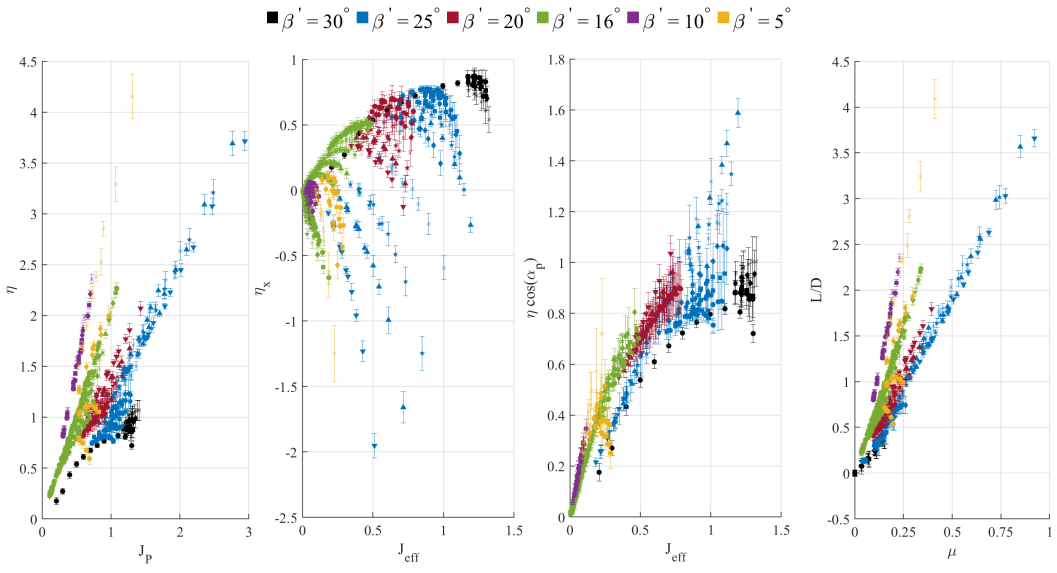


Figure 23: Different propeller and rotor efficiency metrics for CoPTR blades in edgewise conditions.

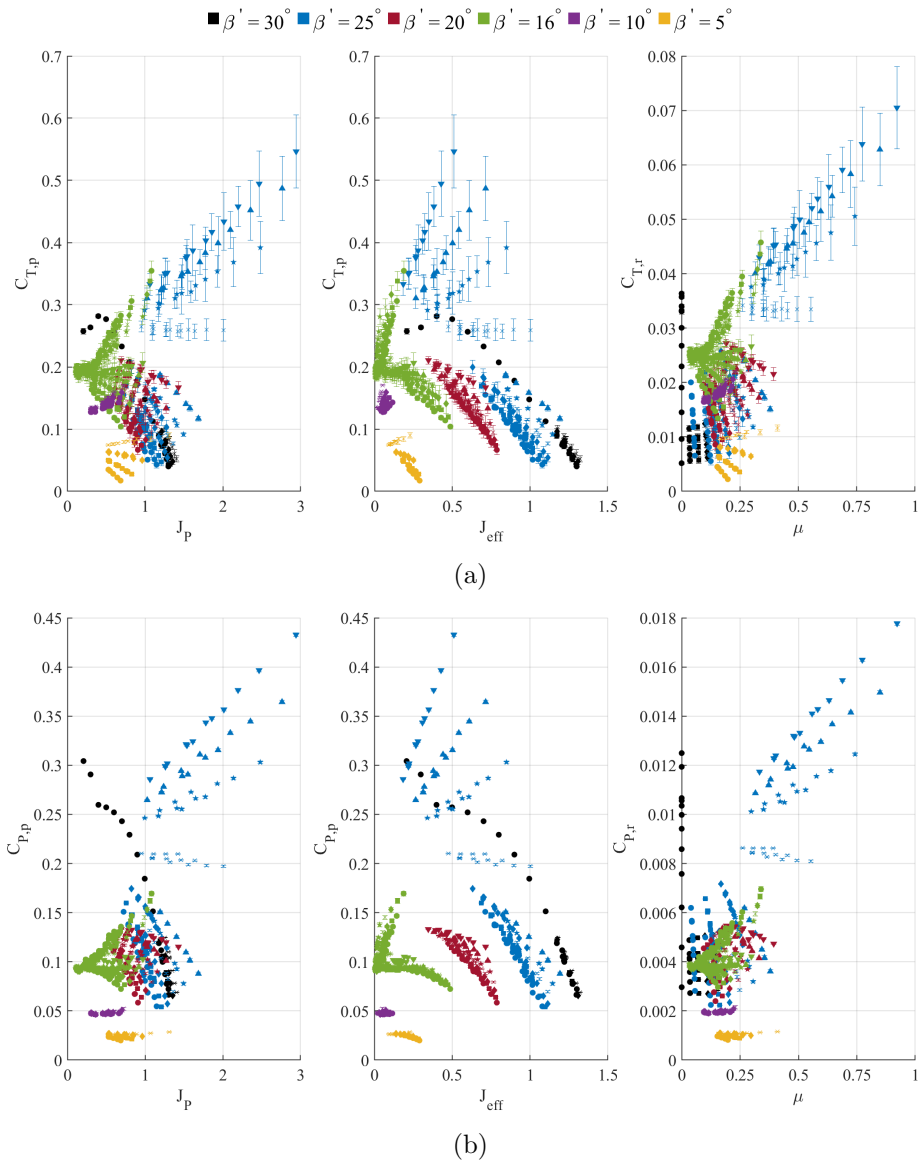


Figure 24: Different propeller and rotor metrics for (a) thrust and (b) power for the CoPTR blades in edgewise conditions.

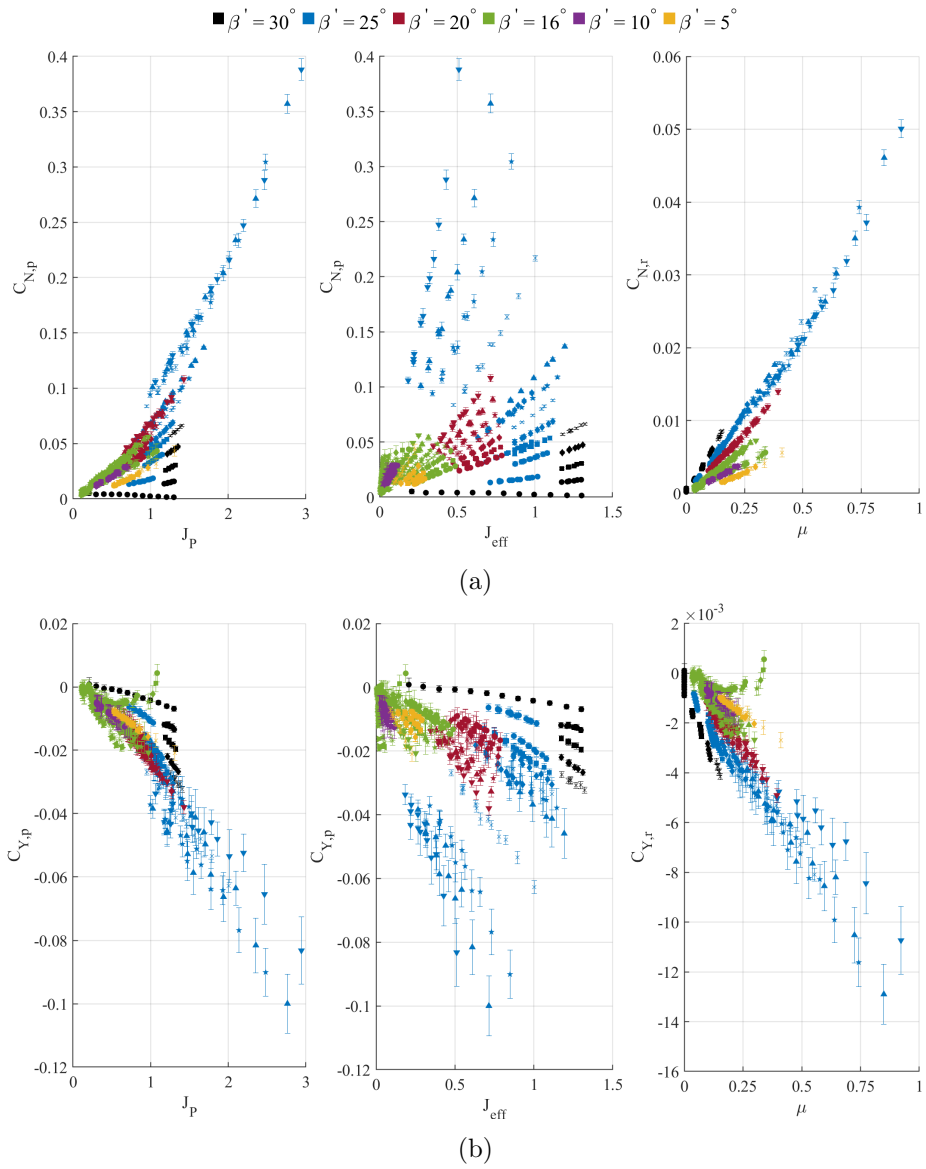
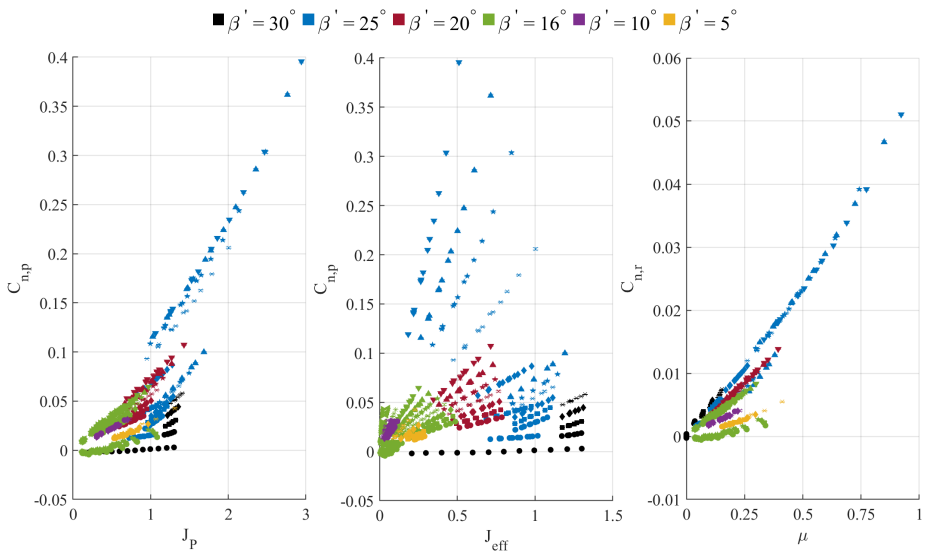
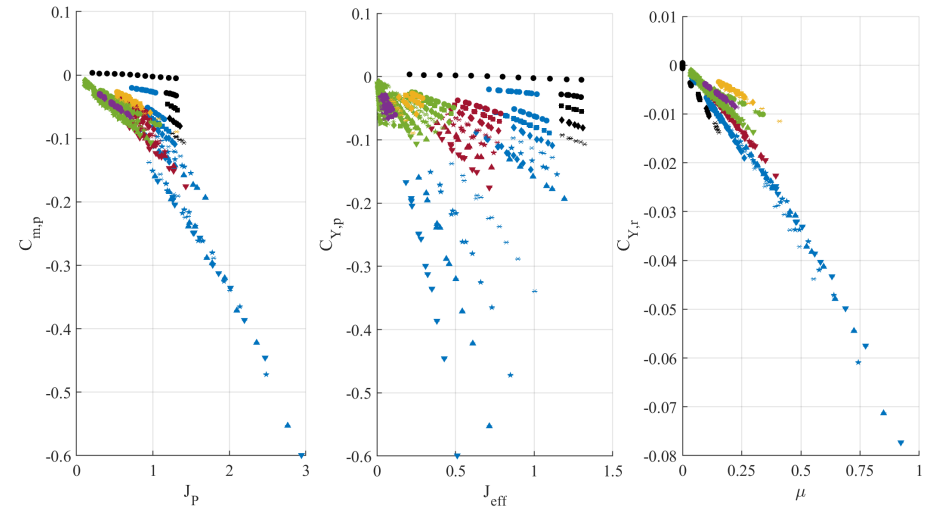


Figure 25: Different propeller and rotor metrics for (a) normal and (b) side forces for the CoPTR blades in edgewise conditions.



(a)



(b)

Figure 26: Different propeller and rotor metrics for (a) yawing and (b) pitching moments for the CoPTR blades in edgewise conditions.

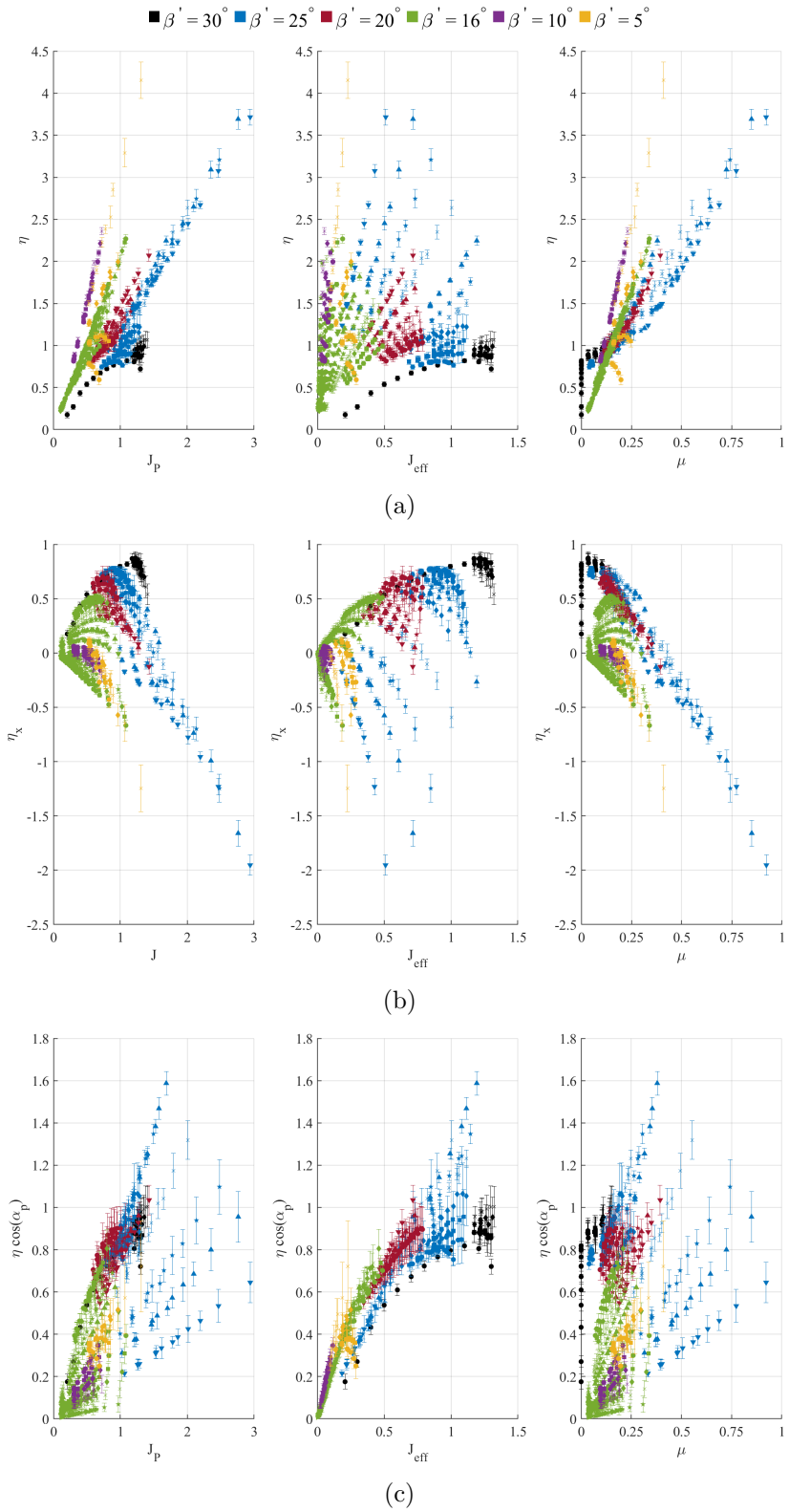


Figure 27: Different propeller metrics for efficiency for the CoPTR blades in edgewise conditions.

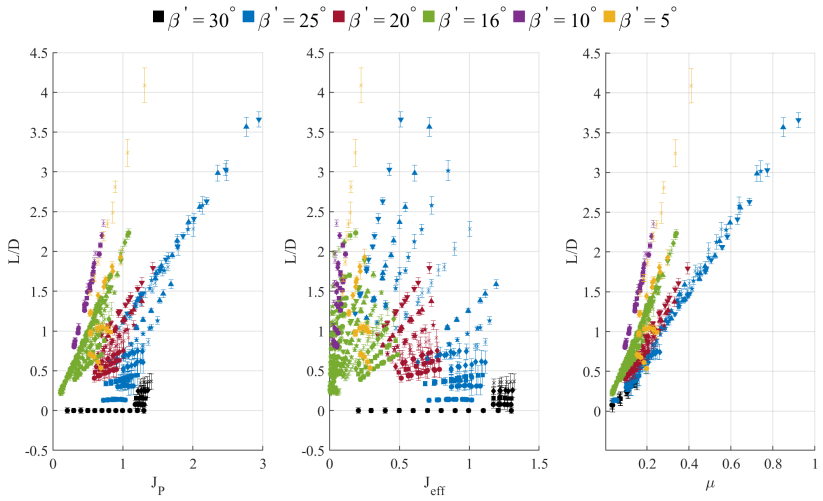


Figure 28: Potential rotor metric for efficiency for the CoPTR blades in edgewise conditions.

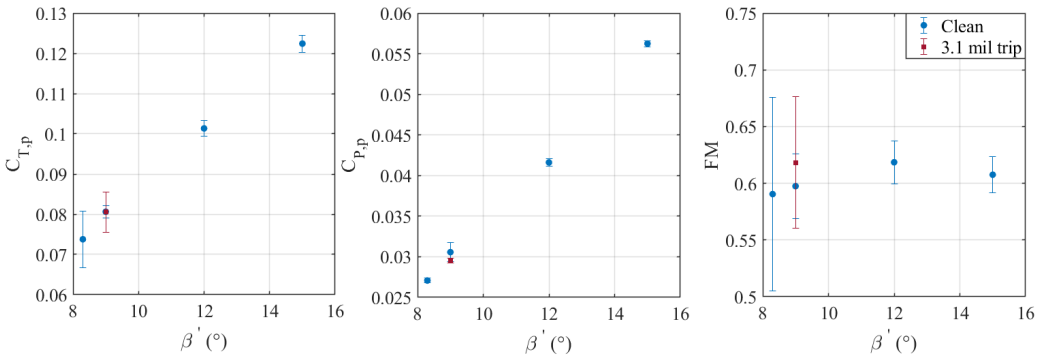


Figure 29: KA1Gen hover performance at M_{tip}=0.300.

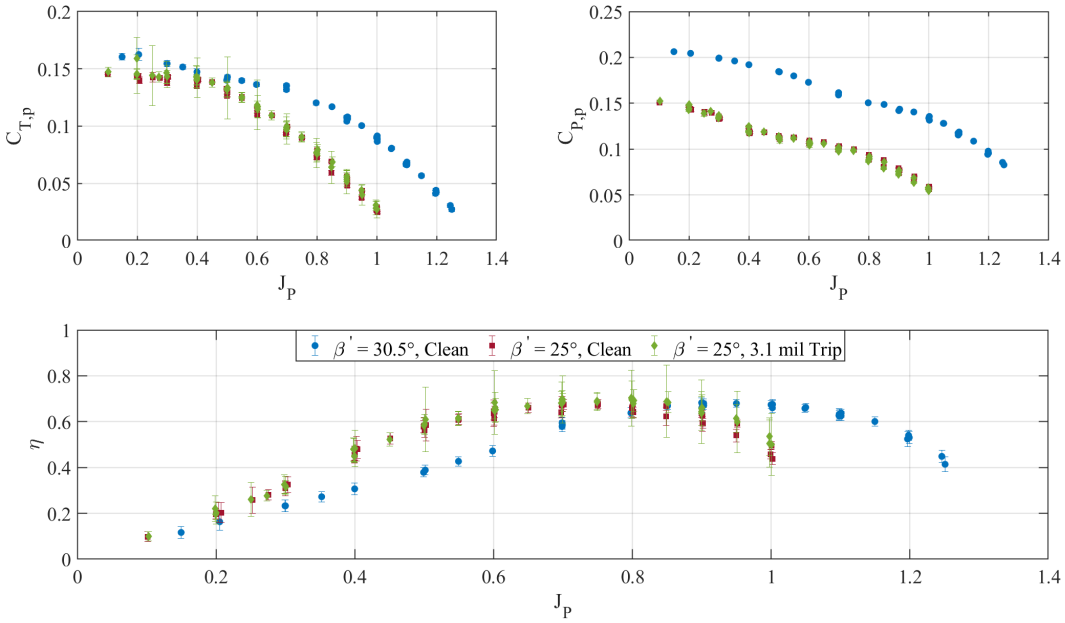


Figure 30: KA1Gen cruise performance for different conditions.

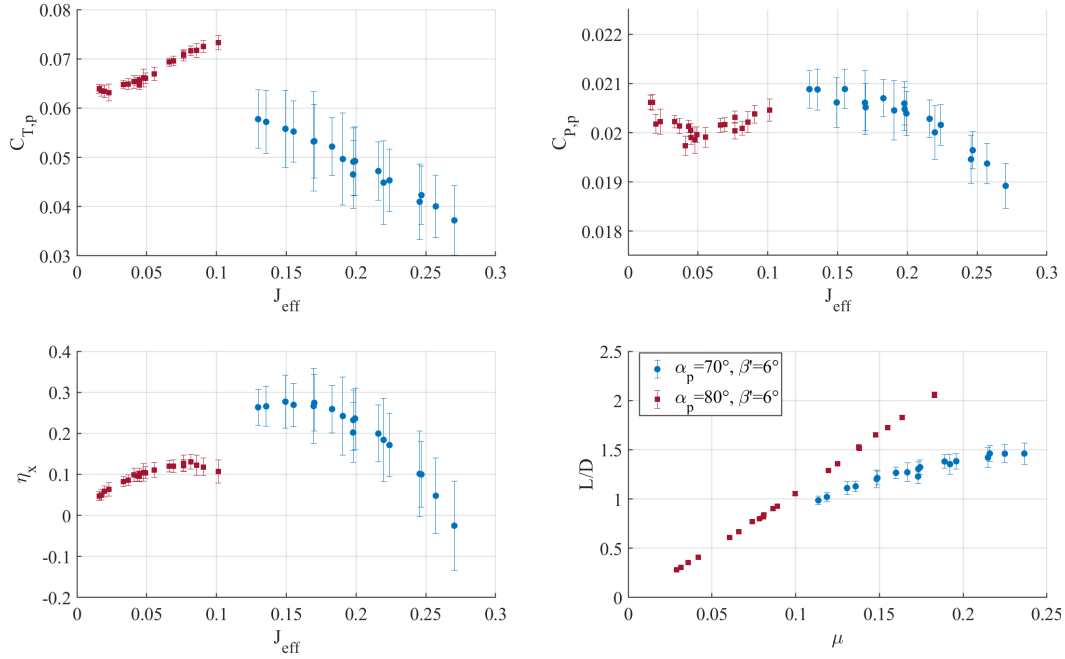


Figure 31: KA1Gen edgewise conditions.

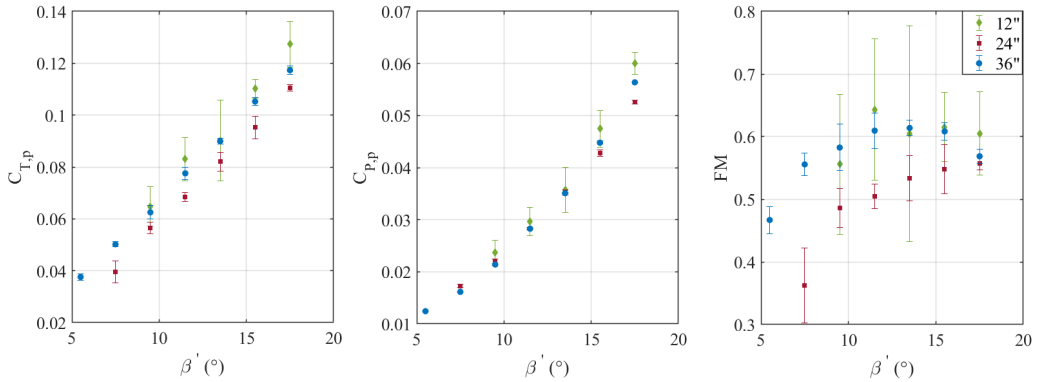


Figure 32: COPR2-G hover performance at M_{tip}=0.300 for different diameters.

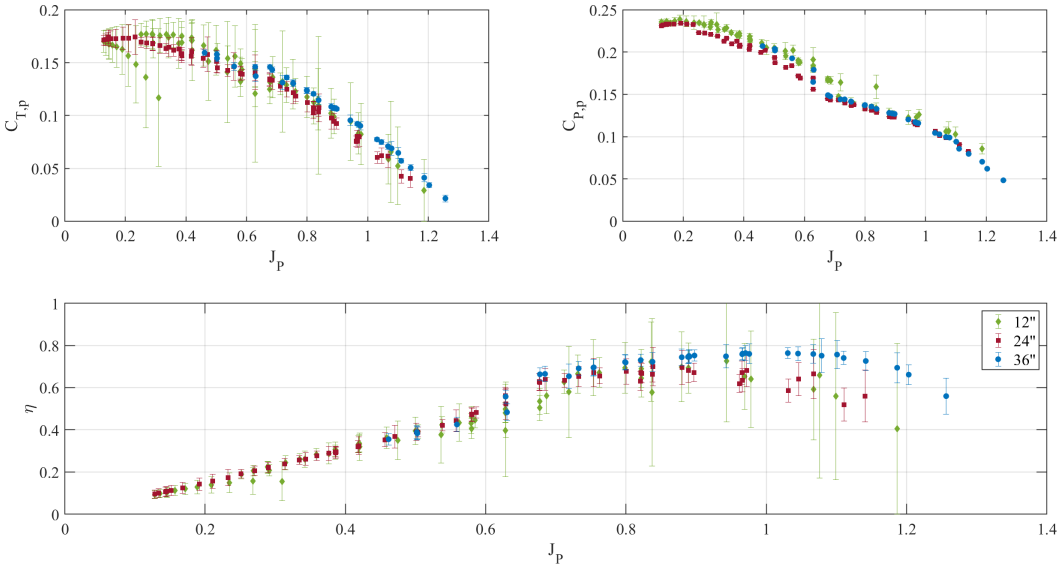


Figure 33: COPR2-G cruise performance for different diameters.

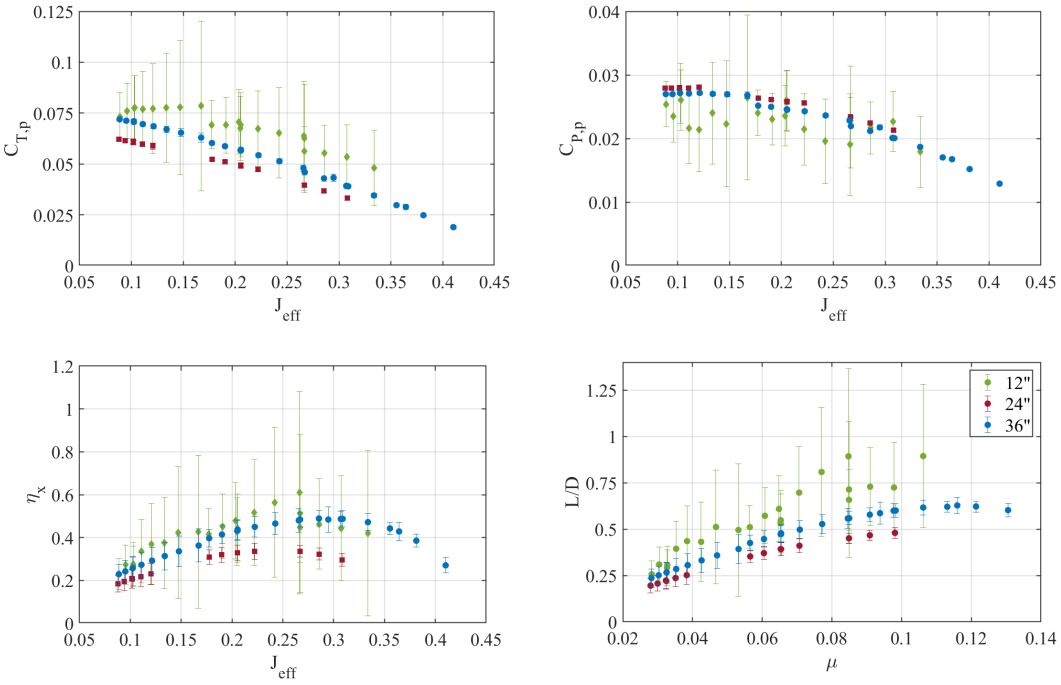


Figure 34: COPR2-G edgewise conditions for different diameters, $\alpha_p = 45°$.

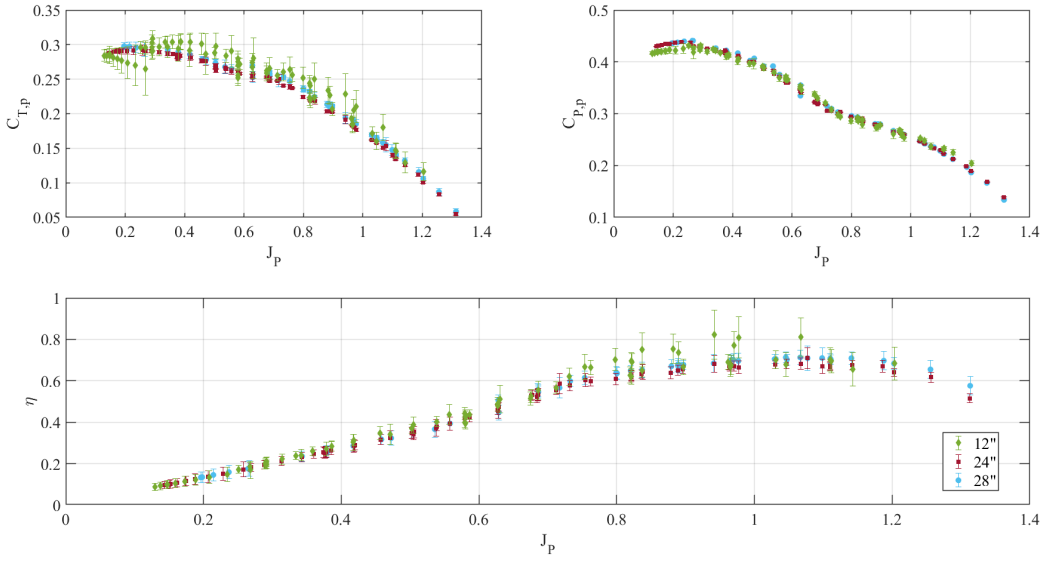


Figure 35: COPR4-G cruise performance for different diameters.

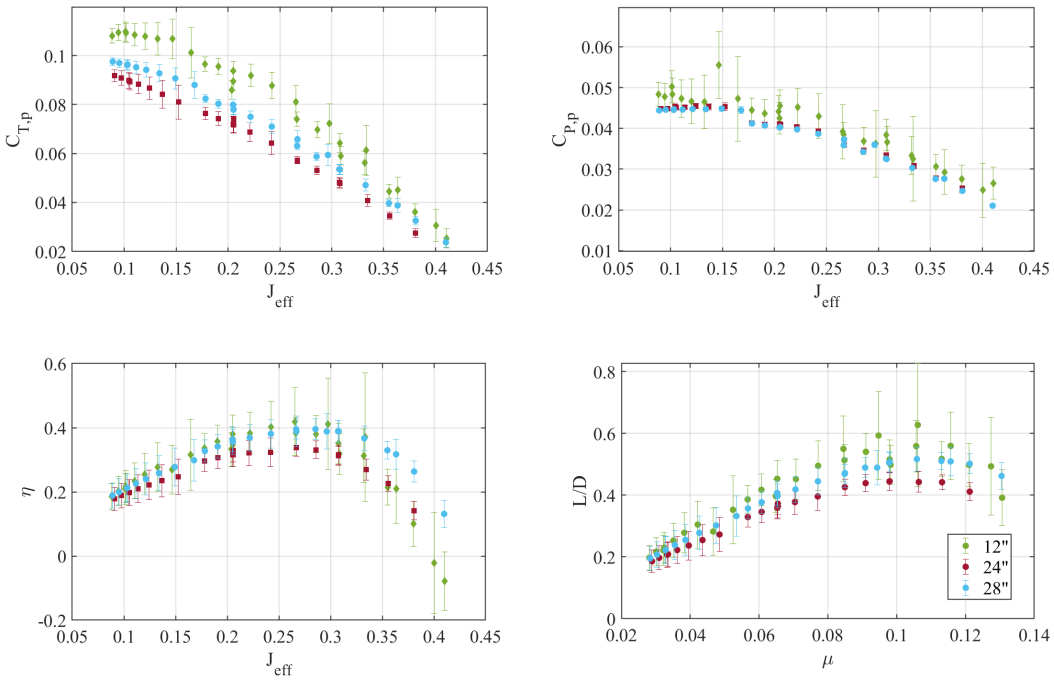


Figure 36: COPR4-G edgewise conditions for different diameters, $\alpha_p = 45°$.

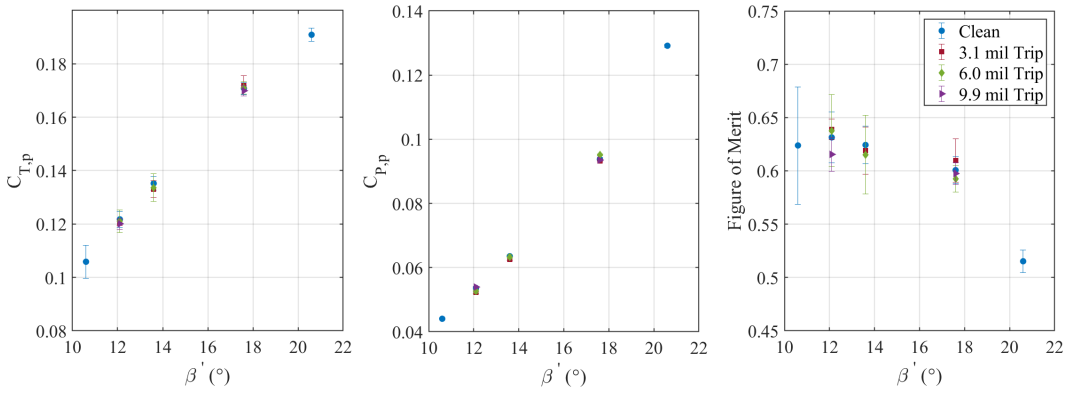


Figure 37: COPR3-L hover performance at M_{tip}=0.300 for different boundary layer trip heights.

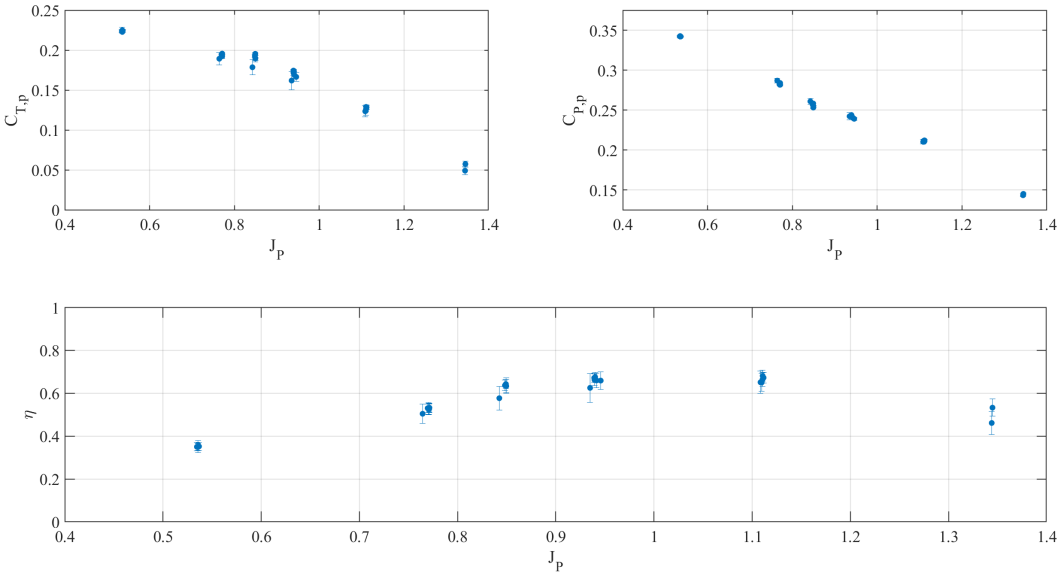
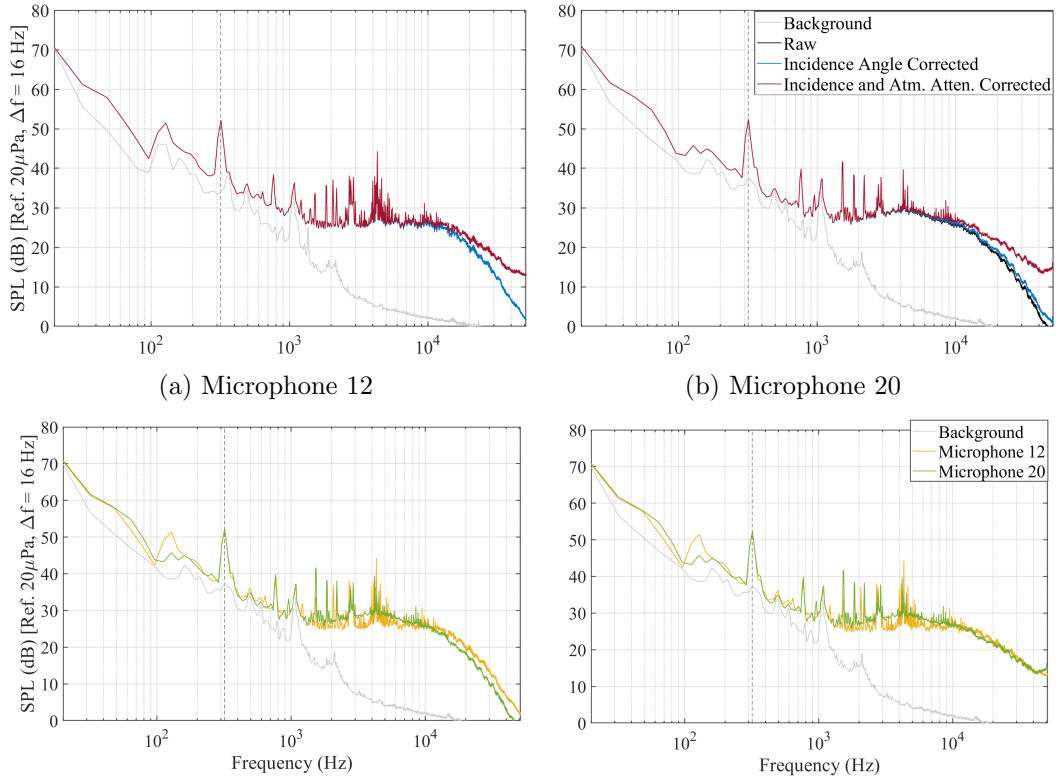


Figure 38: COPR3-L cruise performance without boundary layer tripping.



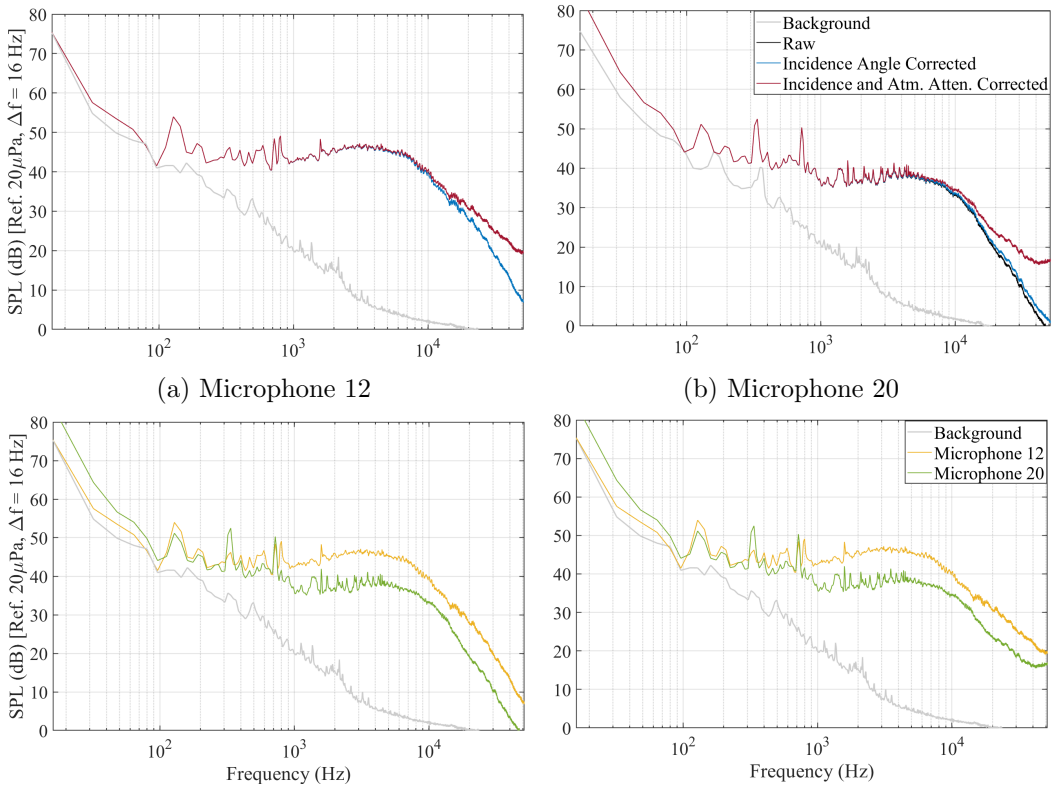
(a) Microphone 12

(b) Microphone 20

(c) Raw Acoustic Spectra

(d) Acoustic Spectra with All Corrections

Figure 39: Acoustic results from CoPTR in hover. Run 0581, $M_{tip} = 0.350$, $\beta' = 16°$.



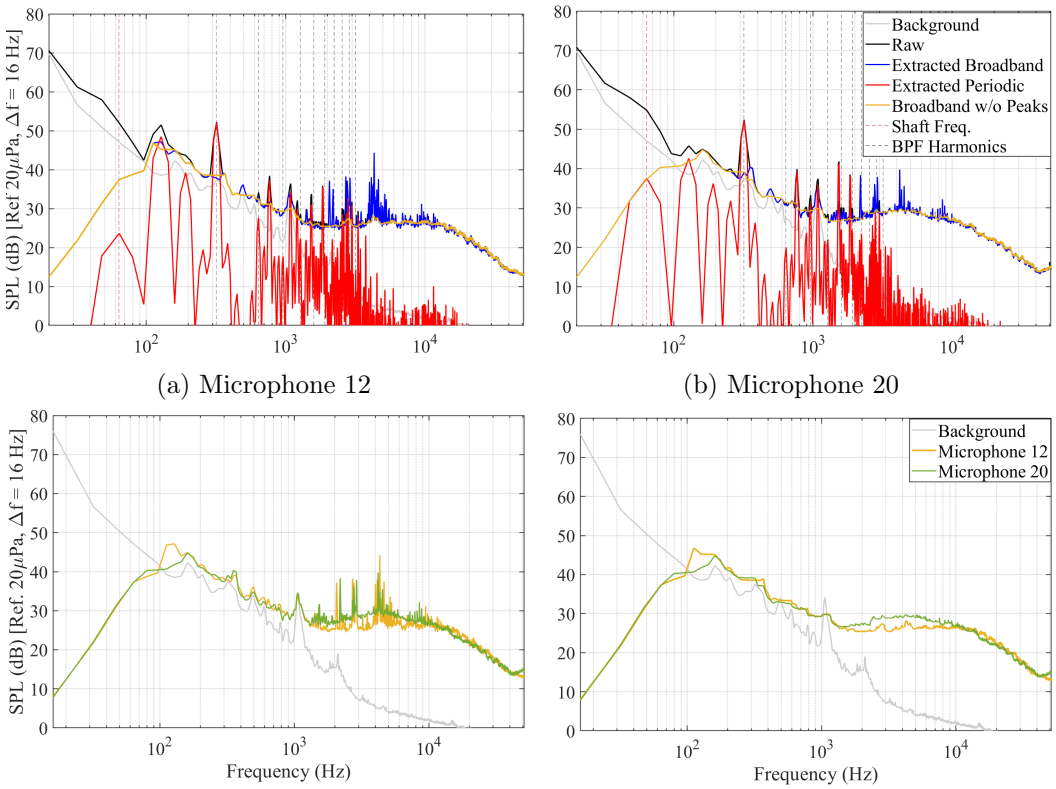
(a) Microphone 12

(b) Microphone 20

(c) Raw Acoustic Spectra

(d) Acoustic Spectra with All Corrections

Figure 40: Acoustic results from CoPTR in edgewise flight. Run 1005, $\beta' = 16°$, $\alpha_p = 88°$.



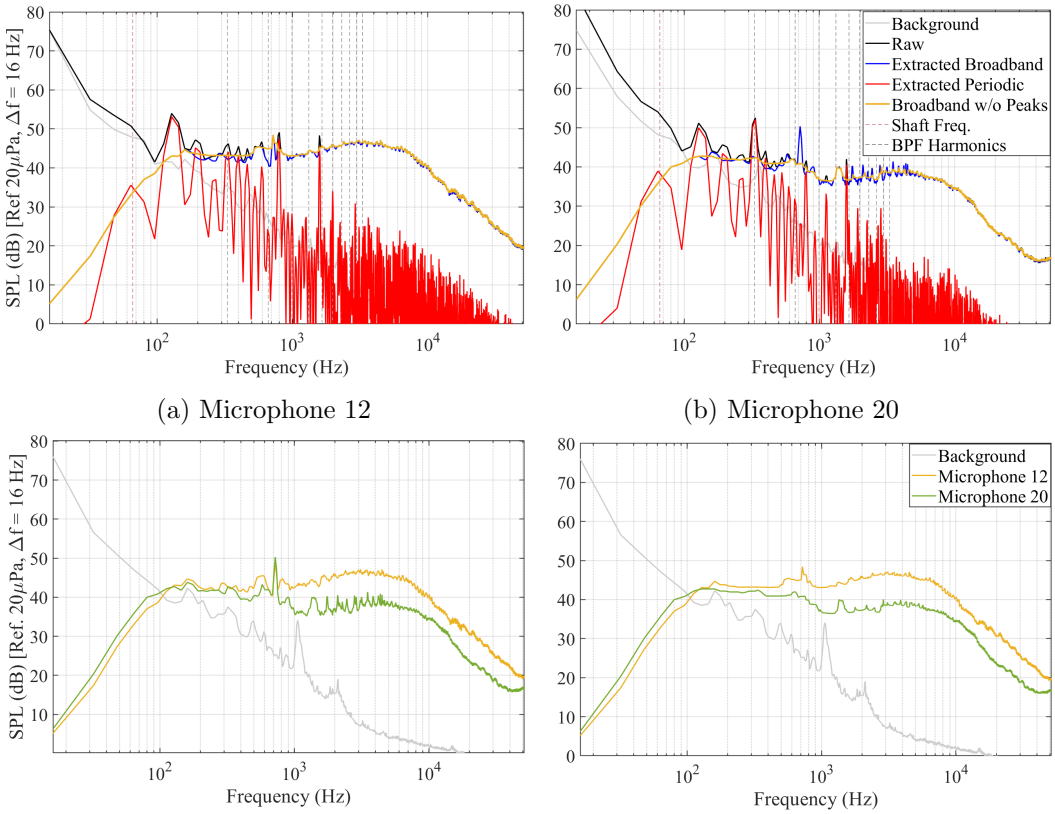
(a) Microphone 12

(b) Microphone 20

(c) Extracted Broadband Spectra

(d) Broadband Spectra with Peaks Removed

Figure 41: Periodic averaging results from CoPTR in hover. Run 0581, $M_{tip} = 0.350$, $\beta' = 16°$.



(a) Microphone 12

(b) Microphone 20

(c) Extracted Broadband Spectra

(d) Broadband Spectra with Peaks Removed

Figure 42: Periodic averaging results from CoPTR in edgewise flight. Run 1005, $\beta' = 16°$, $\alpha_p = 88°$.

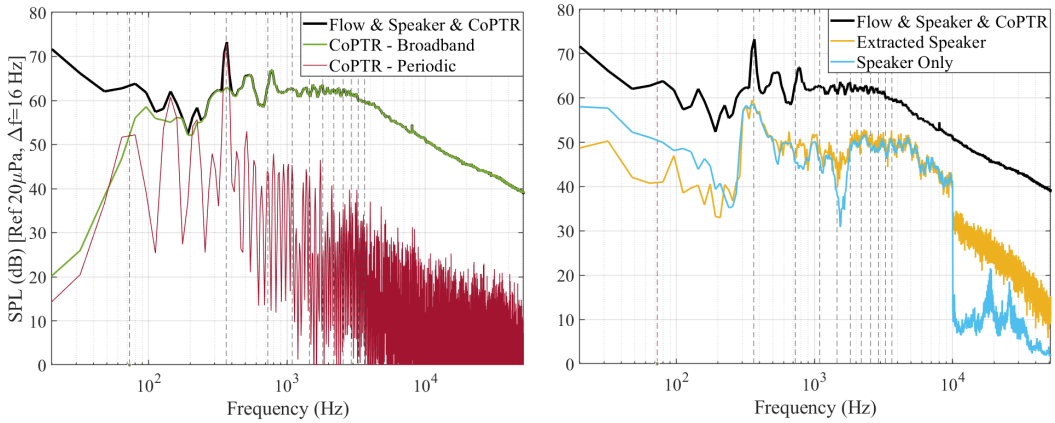
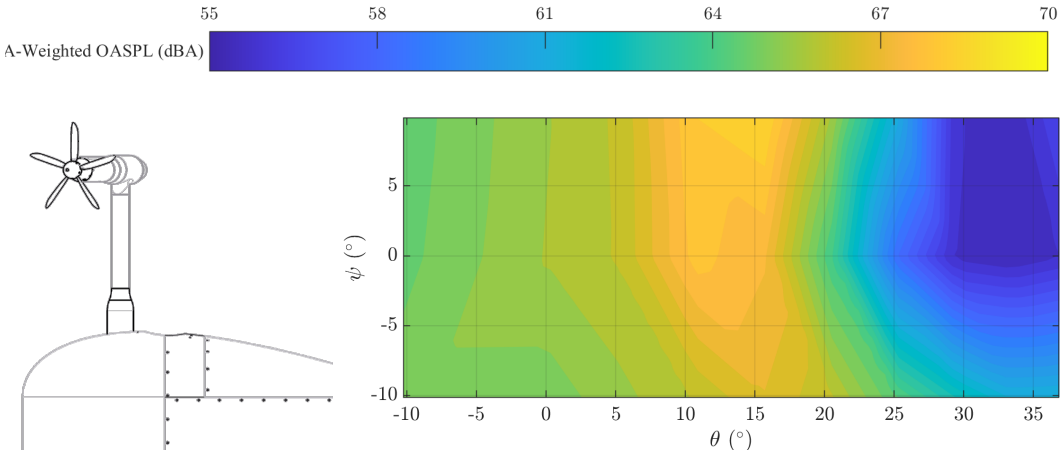
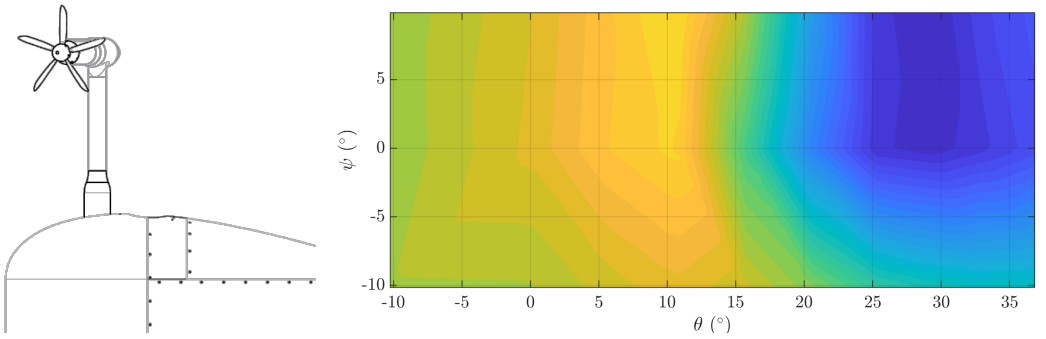


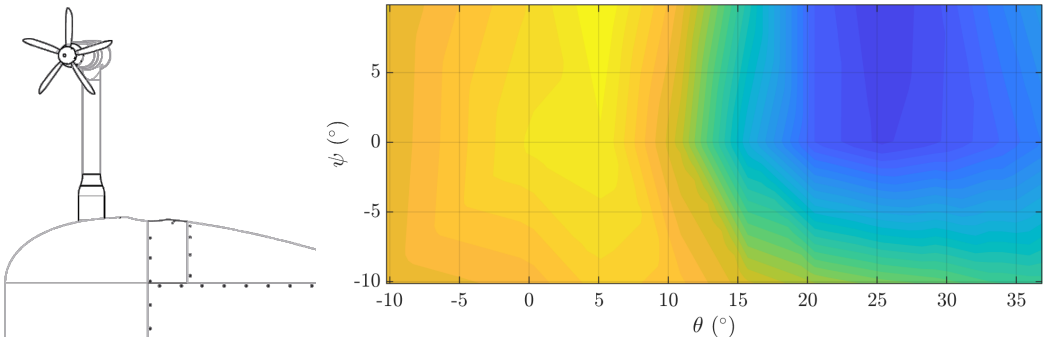
Figure 43: Periodic averaging results from CoPTR in edgewise flight using the tachometer signal (left) and speaker waveform (right) as periods. Run 1075, $\beta' = 16°$, $\alpha_p = 80°$.



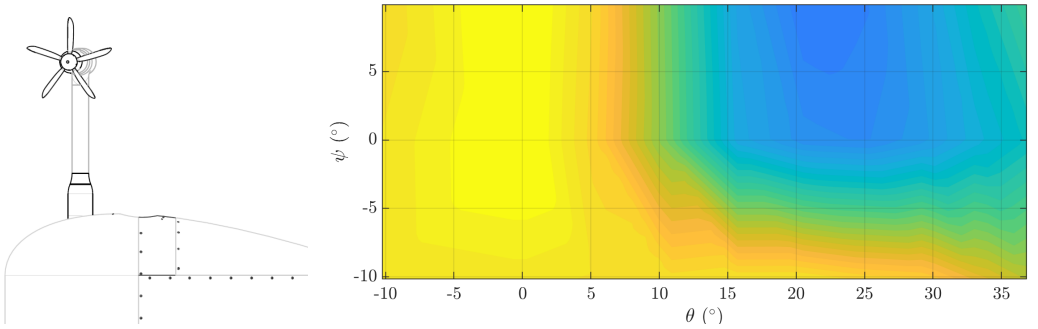
(a) $\alpha_p = 70°$



(b) $\alpha_p = 75°$

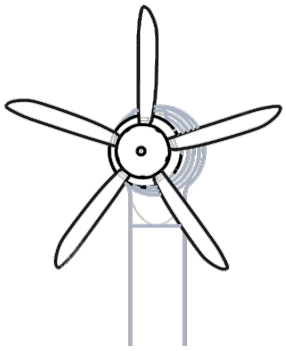


(c) $\alpha_p = 80°$

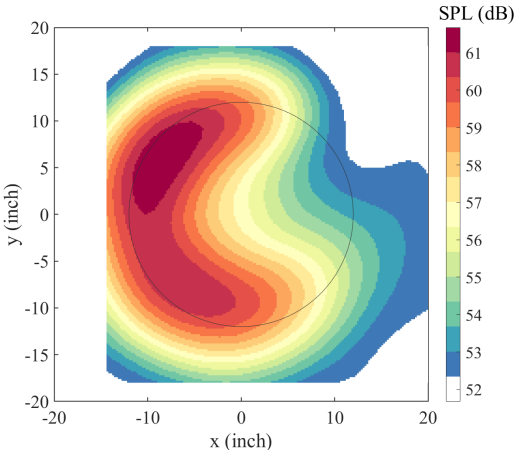


(d) $\alpha_p = 85°$

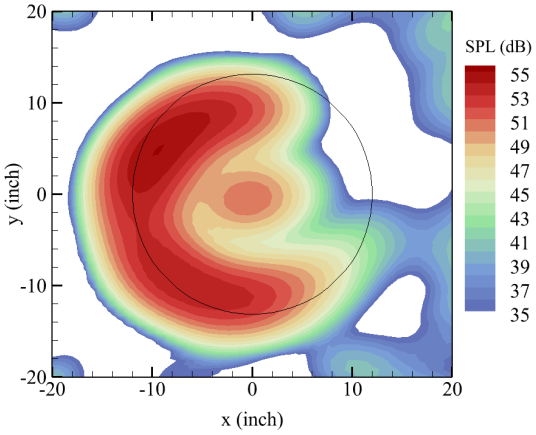
Figure 44: Contours of extracted broadband emissions for CoPTR blades in edgewise flight for $DL = 8$ psf and $M_\infty = 0.015$.



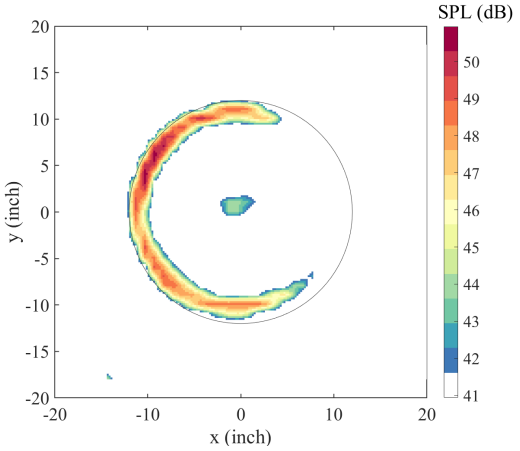
(a) CoPTR, $\alpha_p = 88°$



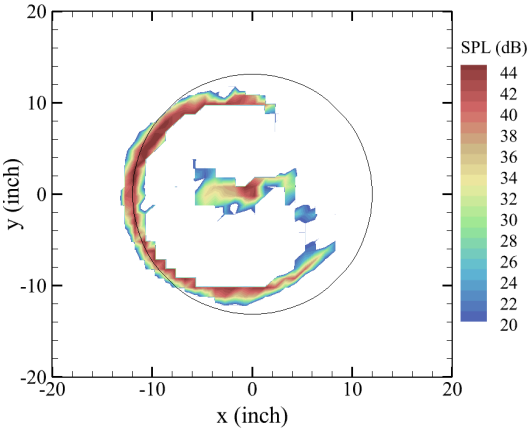
(b) CFDBF



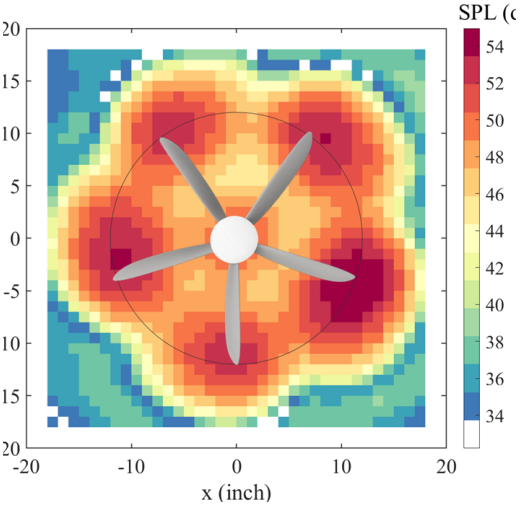
(c) AVEC



(d) DAMAS



(e) AVEC with CLEAN



(f) ROSI

Figure 45: Examples of different beamforming techniques using the CoPTR blades. Run 1004, $\alpha_p = 88°$, DL = 8psf, $M_\infty = 0.015$.

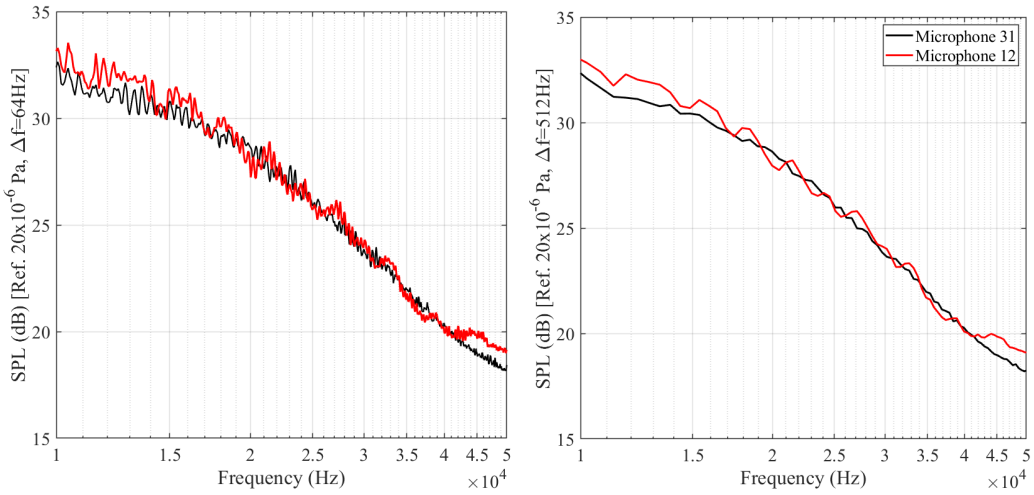
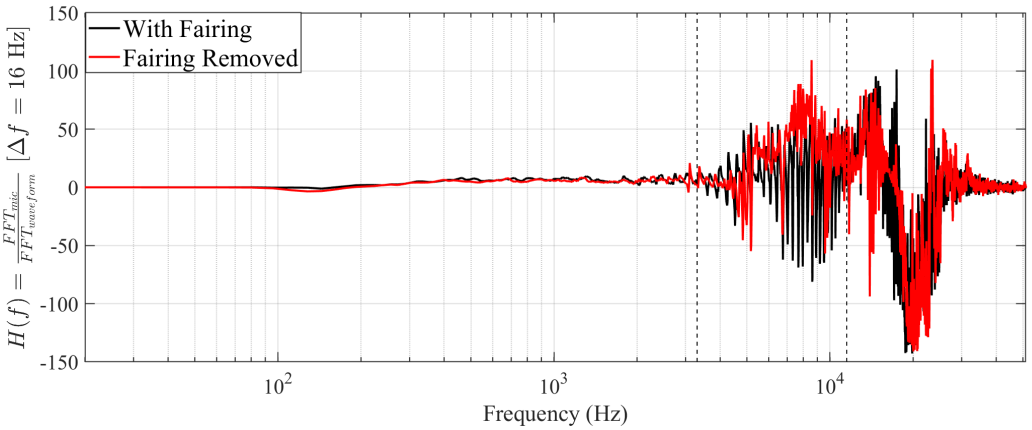
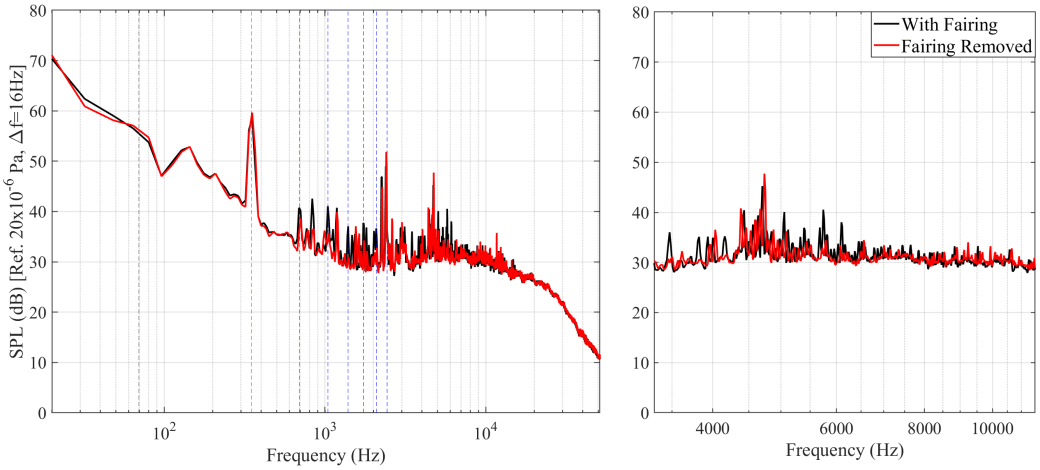


Figure 46: Comparison of similarly-located microphones with and without windscreen cage, plotted in 64 Hz (left) and 512 Hz (right) narrowband bin widths. Hover Run 0581, $M_{tip} = 0.350$, $\beta' = 16°$.

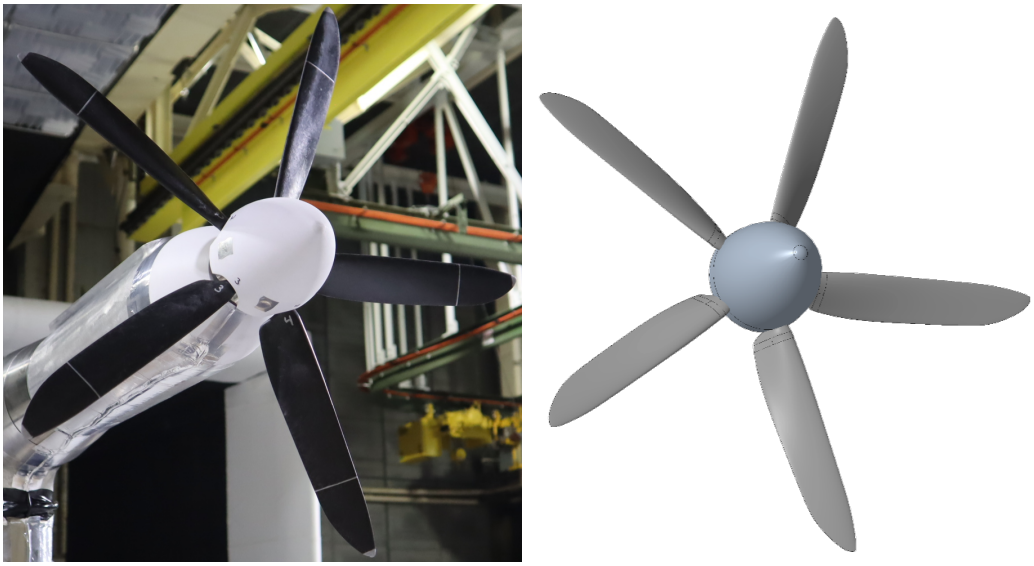


(a) Transfer functions of microphone 12 signal and speaker waveform.



(b) CoPTR blades in hover at $M_{tip} = 0.400$ with and without the fairing. Microphone 12 full spectra (left) and region highlighted by speaker test (right)

Figure 47: Preliminary assessment of reflections off PTS aerodynamic fairing.



(a) (b)

Figure 48: Example of tested geometry (left) and as-designed geometry for data release (right).

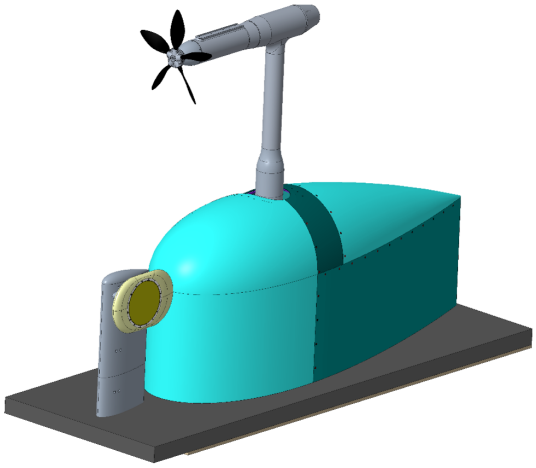


Figure 49: Preliminary CAD geometry of full PTS and inflow speaker source as tested in VLPNT.

REPORT DOCUMENTATION PAGE

Form Approved
OMB No. 0704–0188

The public reporting burden for this collection of information is estimated to average 1 hour per response, including the time for reviewing instructions, searching existing data sources, gathering and maintaining the data needed, and completing and reviewing the collection of information. Send comments regarding this burden estimate or any other aspect of this collection of information, including suggestions for reducing this burden, to Department of Defense, Washington Headquarters Services, Directorate for Information Operations and Reports (0704-0188), 1215 Jefferson Davis Highway, Suite 1204, Arlington, VA 22202-4302. Respondents should be aware that notwithstanding any other provision of law, no person shall be subject to any penalty for failing to comply with a collection of information if it does not display a currently valid OMB control number.
PLEASE DO NOT RETURN YOUR FORM TO THE ABOVE ADDRESS.

1. REPORT DATE *(DD-MM-YYYY)*	2. REPORT TYPE	3. DATES COVERED *(From - To)*
22-09-2026	Technical Memorandum	7/2025–12/2025

4. TITLE AND SUBTITLE
Summary of the Vertical Lift Proprotor Noise Test

5a. CONTRACT NUMBER

5b. GRANT NUMBER

5c. PROGRAM ELEMENT NUMBER

6. AUTHOR(S)
Colin M. Stutz, Nikolas S. Zawodny, and Mary L. Houston

5d. PROJECT NUMBER

5e. TASK NUMBER

5f. WORK UNIT NUMBER

7. PERFORMING ORGANIZATION NAME(S) AND ADDRESS(ES)
NASA Langley Research Center
Hampton, Virginia 23681-2199

8. PERFORMING ORGANIZATION REPORT NUMBER

9. SPONSORING/MONITORING AGENCY NAME(S) AND ADDRESS(ES)
National Aeronautics and Space Administration
Washington, DC 20546-0001

10. SPONSOR/MONITOR'S ACRONYM(S)
NASA

11. SPONSOR/MONITOR'S REPORT NUMBER(S)
NASA–TM–20260007850

12. DISTRIBUTION/AVAILABILITY STATEMENT
Unclassified-Unlimited
Subject Category 71
Availability: NASA STI Program (757) 864-9658

13. SUPPLEMENTARY NOTES
An electronic version can be found at http://ntrs.nasa.gov.

14. ABSTRACT

Urban Air Mobility (UAM) vectored thrust vehicle platforms present the challenges of requiring propulsors to operate in both vertical takeoff and landing (VTOL) as well as axial forward flight. Such vectored thrust vehicles must also contend with the transition flight corridors of departure and approach. Transitional flight conditions create complex aerodynamic interactions, which lead to performance and acoustic characteristics that are difficult to predict numerically. The Vertical Lift Proprotor Noise Test (VLPNT) was a wind tunnel testing campaign in the NASA Langley Research Center's 14- by 22-Foot Subsonic Tunnel aimed at measuring the aerodynamic performance and acoustic behavior of proprotors operating at conditions representative of those from vectored thrust UAM vehicles with articulating propulsors. Another objective of the VLPNT was to conduct a scaling investigation on a subset of the tested proprotor geometries in an effort to identify low-Reynolds number impacts on performance and acoustics. This report documents the test campaign and the resulting data that are available to the community.

15. SUBJECT TERMS
Rotorcraft, Acoustics, Urban Air Mobility

16. SECURITY CLASSIFICATION OF:			17. LIMITATION OF ABSTRACT	18. NUMBER OF PAGES	19a. NAME OF RESPONSIBLE PERSON
a. REPORT	b. ABSTRACT	c. THIS PAGE			STI Information Desk (help@sti.nasa.gov)
U	U	U	UU	75	19b. TELEPHONE NUMBER *(Include area code)* (757) 864-9658